The Kelch13 compartment is a hub of highly divergent vesicle trafficking proteins in malaria parasites

Sabine Schmidt[1,§], Jan Stephan Wichers-Misterek[1,§], Hannah Michaela Behrens[1], Jakob Birnbaum[1], Isabelle Henshall[1], Ernst Jonscher[1], Sven Flemming[1], Carolina Castro-Peña[1], Tobias Spielmann[1,#]

[1] Bernhard Nocht Institute for Tropical Medicine, 20359 Hamburg, Germany
§ contributed equally, order determined alphabetically
# Corresponding author: spielmann@bnitm.de

ORCID:

Sabine Schmidt:	0000-0002-6958-9832
Jan Stephan Wichers-Misterek:	0000-0002-0599-1742
Hannah Michaela Behrens:	0000-0002-7406-7086
Jakob Birnbaum:	0000-0002-1419-522X
Isabelle Henshall:	0000-0002-5906-0687
Ernst Jonscher:	0000-0002-8480-6102
Carolina Castro-Peña:	0000-0002-6878-4951
Tobias Spielmann:	0000-0002-3968-4601

ABSTRACT

Single amino acid changes in the parasite protein Kelch13 (K13) result in reduced susceptibility of *P. falciparum* parasites to Artemisinin and its derivatives (ART). Recent work indicated that K13 and other proteins co-localising with K13 (K13 compartment proteins) are involved in the endocytic uptake of host cell cytosol (HCCU) and that a reduction in HCCU results in ART resistance. HCCU is critical for parasite survival but is poorly understood, with the K13 compartment proteins are among the few proteins so far functionally linked to this process. Here we further defined the composition of the K13 compartment by identifying four novel proteins at this site. Functional analyses, tests for ART susceptibility as well as comparisons of structural similarities using AlphaFold2 predictions of these, and previously identified proteins, showed that canonical vesicle trafficking and endocytosis domains were frequent in proteins involved in resistance and endocytosis, strengthening the link to endocytosis. Despite this, most showed unusual domain combinations and large parasite-specific regions, indicating a high level of taxon-specific adaptation. A second group of proteins did not influence endocytosis or ART resistance and was characterised by a lack of vesicle trafficking domains. We here identified the first essential protein of the second group and showed that it is needed in late-stage parasites. Overall, this work identified novel proteins functioning in endocytosis and at the K13 compartment. Together with comparisons of structural predictions it provides a repertoire of functional domains at the K13 compartment that indicate a high level of adaption of the endocytosis in malaria parasites.

INTRODUCTION

Malaria is one of the deadliest infectious diseases, responsible for an estimated 627 000 deaths and 241 million cases in 2020 [1]. Malaria deaths have been declining in the last two decades [1,2]. One of the factors contributing to this reduction is efficient treatment which currently relies on artemisinin and its derivatives (ART) administered together with a partner drug [3]. However, parasites with a reduced susceptibility to ART have become widespread in South East Asia and now also emerged in Africa [4,5,14–16,6–13]. The reduced effectivity of ART was linked to a delayed parasite clearance in patients that is due to a decreased susceptibility of ring-stage parasites to ART [17,18], leading to recrudescence and treatment failure in patients [19–22]. Decreased susceptibility of ring-stage parasites can be measured *in vitro* using the ring stage survival assay (RSA) [23]. We here refer to this *in vitro* measurable phenomenon as "*in vitro* ART resistance" when the survival of parasites is above 1% in an RSA as previously defined [23]. Point mutations in the gene encoding the

parasite protein Kelch13 (K13) are the main cause for the reduced ART susceptibility of laboratory and field parasite isolates [24,25] and was shown to lead to decreased K13 protein levels [26–30]. This results in reduced hemoglobin uptake via endocytosis, which is assumed to cause less ART activation through hemoglobin degradation products, resulting in the reduced parasite ART susceptibility [26,31].

Endocytosis is a critical process for blood stage growth of malaria parasites. During its asexual development in erythrocytes the parasite uses this process to take up more than two-thirds of the soluble host cell content, which consists almost exclusively of hemoglobin [32–34]. The endocytosed host cell cytosol is transported to the acidic lysosome-like food vacuole (FV), where digestion of hemoglobin results in generation of free heme, which is further converted into nontoxic hemozoin [35,36]. Host cell cytosol uptake (HCCU) provides both space and building blocks (amino acids from digested hemoglobin) for parasite growth [33]. As a consequence, ART resistant parasites are hypersensitive to amino acid restriction, highlighting the importance of endocytosis for parasite growth and its connection to ART resistance [37,38]. Hemoglobin trafficking to the parasite food vacuole is believed to be initiated at membrane invaginations called cytostomes [27,33,39] followed by vesicular transport from the parasite plasma membrane (PPM) to the food vacuole [33,40], likely in an actin-myosin motor dependent manner [39,41–43]. The molecular effectors involved in this process remain poorly characterized and so far only VPS45 [44], the phosphoinositide-binding protein PX1 [45], the host enzyme peroxiredoxin 6 [46] and K13 and some of its compartment proteins (Eps15, AP2µ, KIC7, UBP1) [26] have been reported to act at different steps in the endocytic uptake pathway of hemoglobin. While inactivation of VPS45, PX1 or actin resulted in an accumulation of hemoglobin filled vesicles [43–45], indicative of a block during endosomal transport, no such vesicles were observed upon inactivation of K13 and its compartment proteins [26], suggesting a role of these proteins during initiation of endocytosis.

In previous work we used a quantitative BioID approach to identify proteins in close proximity to K13 and its interactor Eps15 [26]. We designated these proteins K13 interaction candidates (KICs) [26]. As the proteins identified by proximity labelling approaches not only include interactors but also proteins that are located in a close spatial position of the bait [47,48], we will here refer to the collective of these proteins as the "proxiome". We reasoned that due to the high rate of proteins that turned out to belong to the K13 compartment when validating the K13 BioID hits [26], the hit lists of these experiments might contain further proteins belonging to the K13 compartment. Here we identified and functionally analysed further candidates from the K13 proxiome and classify these and previously confirmed K13 compartment proteins. This revealed

100 that the K13 compartment contains proteins suggestive of a highly divergent
101 endocytosis mechanism in malaria parasites but also a second group of proteins with
102 other functions.
103
104 **RESULTS**
105 To identify novel K13 compartment proteins we further exploited previously described
106 proximity-dependent biotinylation experiments that had used K13 or the K13
107 compartment protein Eps15 as bait, selecting enriched proteins not characterized in
108 our previous work [26] (Table S1). In order to do this we excluded proteins that (i) had
109 previously been analysed (ii) were either linked with or had been shown to localise to
110 the inner membrane complex (IMC) (PF3D7_1345600 [49]; PF3D7_0109000 (PhIL1)
111 [50–52]; PF3D7_0717600 (IMC32) [53]; PF3D7_0822900 (PIC2) [54],
112 PF3D7_1018200 (PPP8) [54,55], (iii) are considered typical DiQ-BioID 'contaminants'
113 (PF3D7_0708400 (HSP90) and PF3D7_1247400 (FKBP35) [26,56]), (iv) localised to
114 the apical polar ring in *P. berghei* (PF3D7_1141300 (APR1) [57]), (v) localised to the
115 nucleus PF3D7_1247400 (FKBP35) [58,59], (vi) were linked with the apicoplast
116 (PF3D7_0721100 [60]) or (vi) were also present in BioID experiments using Clathrin
117 heavy chain (CHC) as bait [26] (PF3D7_0408100). These selection criteria resulted in
118 a candidate list of thirteen proteins (PF3D7_1438400 (MCA2), PF3D7_1243400,
119 PF3D7_1365800, PF3D7_1447800, PF3D7_1142100, PF3D7_0103100 (VPS51),
120 PF3D7_1329100 (MyoF), PF3D7_1329500, PF3D7_0405700 (UIS14),
121 PF3D7_0907200, PF3D7_0204300, PF3D7_1117900 and PF3D7_1016200), of
122 which the top ten were chosen as putative K13 compartment proteins for further
123 characterization in this manuscript (Table 1, Table S1).
124
125 **MCA2 is part of the K13 compartment and its truncation confers *in vitro* ART**
126 **resistance**
127 We previously identified metacaspase-2 (MCA2) as one of the top 5 most enriched
128 proteins of the K13 BioID experiments, but endogenous C-terminal tagging with a
129 2xFKBP-GFP-2xFKBP tag was not achieved despite several attempts [26]. By
130 screening of the MalariaGEN *Plasmodium falciparum* Community Project database
131 [61] a SNP at amino acid position 1344 of MCA2 was identified that on its own leads
132 to a stop codon, thereby removing the metacaspase (MCA) domain. According to
133 MalariaGEN, this SNP is found in Africa with a mean prevalence of 52% and in South
134 Asia with 5% prevalence [61]. As a previously generated truncation of MCA2 at amino
135 acid position 57 ($MCA2^{TGD}$-GFP) rendered the parasites resistant to ART as judged
136 by RSAs [26], we generated a second cell line with MCA2 disrupted at the Y1344
137 position ($MCA2^{Y1344Stop}$-GFP^{endo} parasites) (Figure 1A), to assess if this change could

138 mediate resistance in the field. Subsequent analyses of African parasite isolates [62]
139 revealed that this change was always accompanied by a second change in the
140 following base, reverting the stop codon, indicating that this change is not of relevance
141 for resistance in endemic settings. However, as we had not so far been able to localise
142 MCA2, we took advantage of these parasites with the first 1344 amino acids of MCA2
143 fused to GFP to study its localisation. Correct integration of the construct into the *mca2*
144 genomic locus was confirmed by PCR (Figure S1A) and expression of the truncated
145 fusion protein was verified by Western blot (Figure S1A). Live cell imaging of
146 MCA2^{Y1344Stop}-GFP^{endo} parasites revealed expression of MCA2 throughout the
147 intraerythrocytic development cycle, appearing as a single focus in ring stage
148 parasites while two or more foci were detectable in trophozoites and schizonts (Figure
149 1B), in contrast to the predominantly cytosolic localisation of MCA2^{TGD}-GFP (Figure
150 S2A). As this localisation is reminiscent of K13 and KIC localisation [26,63] we
151 generated MCA2^{Y1344Stop}-GFP^{endo} parasite episomally co-expressing mCherry-K13
152 and spatial relationship of MCA2^{Y1344Stop}-GFP and K13 foci was quantified based on
153 fluorescence microscopy (Figure 1C). This analysis showed that 59% of the
154 MCA2^{Y1344Stop} foci overlapped with K13 foci, 20% of the foci showed partial overlap
155 and 21% of the MCA2^{Y1344Stop} foci did not overlap with K13 foci (Figure 1C), indicating
156 a presence of MCA2 at the K13 compartment. In order to exclude an effect of the
157 truncation on MCA2 localisation we generated parasites with an endogenously tagged
158 full length MCA2-3xHA using SLI [63] (Figure S1B) that episomally co-expressed
159 mCherry-K13 and performed immunofluorescence assays (IFA). These experiments
160 confirmed the focal localisation of MCA2. Quantification of the relative localisation of
161 MCA2 and K13 revealed that 44% of MCA2 foci overlapped with K13 (Figure S2B).
162 Partial overlap was observed for 24% of MCA2 foci, whereas 32% MCA2 foci did not
163 overlap with K13. Overall, these findings indicated that MCA2 is a K13 compartment
164 protein but is also found in additional, non-K13 compartment foci.
165
166 MCA2 was recently found to be enriched in BioID experiments with the inner
167 membrane complex (IMC) marker protein PhIL1 [54]. We generated MCA2^{Y1344Stop}-
168 GFP^{endo} parasites episomally co-expressing PhIL1mCherry and analysed schizont
169 stage parasites. Fluorescent imaging with these parasites revealed a close association
170 of MCA2^{Y1344Stop}-GFP foci with the IMC at the periphery of the newly formed
171 merozoites (Figure 1D), as previously observed for K13 [54]. Of note, no
172 MCA2^{Y1344Stop}-GFP foci were observed in free merozoites (Figure 1D). This data
173 indicates that MCA2 and the K13 compartment - as previously suggested [27,54] - are
174 found proximal to the IMC in schizonts.

175
176 We previously showed that a truncation of MCA2 at amino acid position 57 results in
177 significantly reduced *in vitro* parasite proliferation [26]. Proliferation assays with the
178 MCA2^{Y1344Stop}-GFP^{endo} parasites which express a larger portion of this protein yet still
179 lack the MCA domain (Figure 1A) indicated no growth defect in these parasites
180 compared to 3D7 wild type parasites (Figure 1E). Hence, the MCA domain in MCA2
181 does not appear to be needed for efficient *in vitro* blood stage growth.
182
183 Next, we performed a ring-stage survival assay (RSA) which revealed that the
184 truncation of MCA2 at amino acid position Y1344 resulted in a reduced sensitivity to
185 ART (Figure 1F). The mean parasite survival rate was 1.64%, which is above the
186 defined ART resistance cut-off value of 1% [23], but lower than the ~5% survival rate
187 of the MCA2-TGD parasites [26]. Overall, our results establish MCA2 as a member of
188 the K13 compartment that has a function needed for optimal parasite growth during
189 the intra-erythrocytic development cycle and that confers *in vitro* ART resistance when
190 impaired. Its function facilitating for efficient parasite growth and, to a lesser extent, its
191 influence on ART resistance were independent of its MCA domain.
192
193 **MyosinF is involved in host cell cytosol uptake and associated with the K13**
194 **compartment**
195 The identification of MyosinF (MyoF) in the K13 compartment DiQ-BioIDs could
196 indicate an involvement of actin/myosin in endocytosis in malaria parasites as
197 suspected based on actin inhibitor studies [41,43,64]. We therefore analysed its
198 location in the cell. For this, we first generated transgenic parasites expressing a C-
199 terminally 2xFKBP-GFP-2xFKBP tagged version expressed from its original locus
200 using SLI (Figure S1C). Expression and localisation of the fusion protein was analysed
201 by fluorescent microscopy. The tagged MyoF was detectable as foci close to the food
202 vacuole from late ring stage / young trophozoite stage onwards, while in schizonts
203 multiple MyoF foci were visible (Figure 2A). This expression pattern is in agreement
204 with its transcriptional profile [65,66]. A similar localisation was observed in a cell line
205 expressing MyoF with a smaller tag (MyoF-2xFKBP-GFP) from its endogenous locus
206 (Figure S1D, Figure S3A). The proximity of the MyoF foci to the food vacuole was also
207 evident by co-localisation with an episomally expressed food vacuole marker
208 (P40PXmCherry) (Figure 2B). Next, we used the MyoF-2xFKBP-GFP-2xFKBP^{endo}
209 parasites to generate a cell line episomally co-expressing mCherry-K13 (Figure 2C).
210 Quantification from live fluorescence images revealed that 8% of MyoF foci overlapped
211 with K13 foci, 12% showed a partial overlap, 36% were close together (touching but
212 not overlapping), while 44% of MyoF foci were further away from K13 foci (Figure 2C).

213 As the GFP-tagging of MyoF appeared to have some effect on the parasite (see
214 below), we validated the MyoF localisation by generating parasites with an
215 endogenously 3xHA-tagged MyoF (MyoF-3xHA^{endo} parasites) using SLI (Figure S1E)
216 and episomally co-expressed mCherry-K13. IFA confirmed the focal localisation of
217 MyoF and its spatial association with mCherry-K13 foci (Figure S3B). We also
218 detected MyoF signal in ring stage parasites (Figure S3B). As we did not detect the
219 GFP-tagged version in rings, this might indicate low level expression of MyoF in ring
220 stage parasites. Taken together these results show that MyoF is in foci that are
221 frequently close or overlapping with K13, indicating that MyoF is found in a regular
222 close spatial association with the K13 compartment and at times overlaps with that
223 compartment.
224
225 During routine *in vitro* culturing we noticed that MyoF-2xFKBP-GFP-2xFKBP^{endo}
226 parasites grew poorly and subsequent flow cytometry-based proliferation assays
227 revealed a mean relative growth of 36.7% compared to 3D7 wild type parasites after
228 two replication cycles (Figure 2D). These results indicated that C-terminal 2xFKBP-
229 GFP-2xFKBP tagging of MyoF impaired its function and that this protein has an
230 important role for the growth of asexual blood stages. We therefore generated MyoF-
231 2xFKBP-GFP-2xFKBP^{endo} parasites episomally expressing a nuclear mislocaliser
232 (1xNLS-FRB-mCherry) in order to conditionally inactivate it using knock-sideways.
233 This system allows the conditional mislocalisation of a protein from its site of action
234 into the nucleus upon addition of rapalog [63,67,68]. Assessment of mislocalisation
235 efficacy by fluorescent microscopy at 1 hour post induction and 22 hours post induction
236 revealed only partial mislocalisation of MyoF-2xFKBP-GFP-2xFKBP to the nucleus
237 with some MyoF remaining at foci close to the food vacuole (Figure 2E). Despite the
238 only partial inactivation of MyoF by knock sideways, flow cytometry-based proliferation
239 assays revealed a 40.5% reduced parasitemia after two replication cycles upon
240 addition of rapalog compared to control parasites without rapalog, while such an effect
241 was not observed for 3D7 wild type parasites upon addition of rapalog (Figure 2F,
242 Figure S3D). Hence, conditional inactivation of MyoF further reduced growth despite
243 the fact that the tag on MyoF already led to a substantial growth defect.
244
245 Inspection of the MyoF-2xFKBP-GFP-2xFKBP^{endo}, compared to 3D7 wild type-
246 trophozoites, revealed an increased number of vesicles in the parasite cytoplasm
247 (Figure 2G), resembling the phenotype observed after inactivation of VPS45 [44]. This
248 was even more pronounced upon inactivation of MyoF (Figure 2G), suggesting this is
249 due to a reduced function of MyoF. Additionally, we directly tested for an effect of MyoF
250 inactivation on HCCU using a 'bloated food vacuole assay' [44]. For this we incubated
251 parasites upon MyoF inactivation (and control parasites without rapalog) with the

252 protease inhibitor E64 [69]. In the presence of E64, newly internalized hemoglobin
253 cannot be degraded and accumulates in the food vacuole, resulting in bloated food
254 vacuoles. While 88% of control parasites developed bloated food vacuoles, only 52%
255 of the cells with inactivated MyoF showed a bloated food vacuole (Figure 2H, Figure
256 S3E), indicating that less hemoglobin reached the food vacuole upon inactivation of
257 MyoF.
258
259 Finally, we also tested if inactivation of MyoF has an effect on *in vitro* ART resistance.
260 RSAs [23] revealed no significant increase in parasite survival upon MyoF inactivation
261 with neither 12 h nor 24 h rapalog pre-incubation (Figure 2I, Figure S3F). Overall, our
262 results indicate a close association of MyoF foci with the K13 compartment and a role
263 of MyoF in endocytosis albeit at a different step than K13 compartment proteins.
264
265 **KIC11 is a K13 compartment associated protein important for asexual parasite**
266 **proliferation, but not involved in endocytosis or ART resistance**
267 PF3D7_1142100, currently annotated as 'conserved Plasmodium protein, unknown
268 function', was renamed K13 interacting candidate 11 (KIC11), following the previously
269 established nomenclature for potential K13 compartment proteins [26]. In order to test
270 whether KIC11 is a member of the K13 compartment or not, we first generated
271 transgenic parasites expressing it as a C-terminally 2xFKBP-GFP-2xFKBP tagged
272 fusion protein from the original genomic locus using SLI (KIC11-2xFKBP-GFP-
273 2xFKBP^{endo} parasites). Correct genomic modification of the *kic11* locus was verified
274 by PCR (Figure S1F). The tagged KIC11 was poorly detectable in rings (preventing a
275 meaningful assessment of localisation) but showed several foci from the trophozoite
276 stage onwards, while in schizonts many KIC11-2xFKBP-GFP-2xFKBP foci were
277 visible (Figure 3A). Next, we generated KIC11-2xFKBP-GFP-2xFKBP^{endo} parasites
278 episomally co-expressing mCherry-K13. Fluorescence microscopy showed overlap of
279 the foci of both fusion proteins in trophozoites, while in schizonts only some foci
280 overlapped (Figure 3B). We conclude that KIC11 is a protein located at the K13
281 compartment in trophozoites and to a lesser extent in schizonts.
282
283 In order to assess the importance of KIC11 for parasite proliferation, we generated
284 KIC11-2xFKBP-GFP-2xFKBP^{endo} parasites episomally co-expressing the nuclear
285 mislocaliser 1xNLS-FRB-mCherry, enabling conditional inactivation by knock-
286 sideways. Addition of rapalog resulted in efficient mislocalisation of KIC11-2xFKBP-
287 GFP-2xFKBP into the nucleus 4 and 16 hours post induction (Figure 3C). Assessment
288 of parasite proliferation by flow-cytometry over two developmental cycles revealed a
289 mean relative growth of 10.3% compared to control parasites, indicating an important
290 function of KIC11 for asexual parasite proliferation (Figure 3D, Figure S4A). This

interpretation was supported by several unsuccessful attempts to generate a cell line with a truncated *kic11* using the SLI-TGD system [63].

To better characterize the growth phenotype of the KIC11 knock-sideways, we added rapalog to tightly synchronised parasites at different time points (4, 24, and 32 hpi) and monitored parasite growth by flow cytometry. Additionally, we quantified parasite stage in Giemsa smears at 6, 24, 32, 40, 48, 72, and 96 hpi. While no effect on parasitemia and stage distribution was observed during growth in the first cycle, a reduced number of newly formed ring stage parasites was obvious at 48 hpi for all three rapalog addition time points, indicating an effect on parasite viability in late schizont or merozoites but no other stage (Figure 3E-F, Figure S4B). As the trophozoites with inactivated KIC11 developed into schizonts without morphological differences to controls (Figure 3F), KIC11 does not appear to be needed for endocytosis. To directly address this we tested if inactivation of KIC11 influences *in vitro* ART resistance (based on RSA) or endocytosis (using bloated food vacuole assays), but no significant differences were observed (Figure 3G-I, Figure S4C,D). Overall, our results indicate that KIC11 is part of the K13 compartment in trophozoites and that it has an important role for asexual parasite proliferation in late-stage parasites, which is in contrast to previously characterised essential K13 compartment proteins. These findings indicate that there are also K13 compartment proteins that have an important function not related to endocytosis.

KIC12 is located in the nucleus and at the K13 compartment and is involved in endocytosis but not in ART resistance

PF3D7_1329500, currently annotated as ‘conserved protein, unknown function’ was renamed K13 interacting candidate 12 (KIC12). In order to test whether KIC12 is a member of the K13 compartment or not, we first generated transgenic parasites expressing C-terminally 2xFKBP-GFP-2xFKBP tagged KIC12 from its original genomic locus (KIC12-2xFKBP-GFP-2xFKBP^{endo} parasites) (Figure S1G). Expression and localisation of tagged KIC12 was analysed by fluorescent microscopy. KIC12 was detectable in the nucleus in ring stage parasites. In trophozoites foci in the parasite periphery (Figure 4A, white arrows) were observed in addition to the signal in the nucleus (Figure 4A, light blue arrows). In schizonts these foci were not present anymore. Instead, only the nuclear signal and a faint uniform cytoplasmic GFP signal was detected in early schizonts and these signals both disappeared in later schizonts (Figure 4A, Figure S5A). In line with this expression pattern, the *kic12* transcriptional profile indicate mRNA levels peaks in merozoites and early ring-stage parasites and no RNA expression in trophozoites and schizonts [65,66,70]. Next, we generated KIC12-2xFKBP-GFP-2xFKBP^{endo} parasites episomally co-expressing mCherry-K13

330 which revealed an overlap of the KIC12 foci in the cell periphery with the K13 foci in
331 trophozoites (Figure 4B, Figure S5A). In rings, the K13 foci did not overlap with KIC12,
332 in agreement with the exclusively nuclear localisation of KIC12 in that stage (Figure
333 4B). We conclude that KIC12 is a protein with a dual location in the nucleus and the
334 K13 compartment in trophozoites.
335
336 In order to assess the importance of KIC12 for parasite proliferation, we generated
337 KIC12-2xFKBP-GFP-2xFKBP^{endo} enabling conditional inactivation by knock-sideways
338 using a nuclear (1xNLS-FRB-mCherry) mislocaliser. Efficient mislocalisation of KIC12-
339 2xFKBP-GFP-2xFKBP into the nucleus and absence of KIC12 foci in the cytoplasm of
340 trophozoites upon addition of rapalog was confirmed by microscopy at 4 and 16 hours
341 post induction (Figure 4C). Assessing parasite proliferation after knock sideways of
342 KIC12 showed a mean relative growth of 37.0% compared to control parasites after
343 two development cycles, indicating an important function of KIC12 for asexual parasite
344 proliferation (Figure 4D; Figure S5B). Due to the dual localisation of KIC12 we also
345 generated KIC12-2xFKBP-GFP-2xFKBP^{endo} parasites episomally co-expressing an
346 alternative mislocaliser (Lyn-FRB-mCherry) [63], enabling conditional inactivation of
347 the nuclear pool of KIC12-2xFKBP-GFP-2xFKBP by mislocalisation to the parasite
348 plasma membrane (PPM), an approach previously shown to be suitable for efficiently
349 inactivate nuclear proteins [63,71]. Induction of KIC12 mislocalisation to the PPM
350 resulted in a loss of KIC12 in the nucleus 4 hours post induction (Figure 4E). Foci were
351 still detected in the parasite periphery and it is unclear whether these remained with
352 the K13 compartment or were also in some way affected by the Lyn-mislocaliser.
353 Parasite proliferation assays revealed a growth defect of 49.2%, compared with 37.0%
354 of the nuclear mislocalisation approach (Figure 4D; Figure S5C). The small difference
355 between the two mislocalisers and the unclear influence on PPM foci of the Lyn
356 mislocaliser does not permit a clear interpretation in regard to the functional
357 importance of KIC12 at the two locations (nucleus and K13 compartment) of KIC12.
358 However, these data overall confirm that KIC12 is important for efficient growth of
359 asexual blood stages. The importance of KIC12 for asexual parasite proliferation was
360 further supported by failure to obtain a cell line with a truncated *kic12* using the SLI-
361 TGD system.
362
363 Based on the presence at the K13 compartment in trophozoites, we tested the effect
364 of KIC12 inactivation on endocytosis. Bloated food vacuole assays showed that >99%
365 of control parasites developed bloated food vacuoles, while only 49,3% (NLS
366 mislocaliser) or 72.9% (Lyn mislocaliser) of the cells with inactivated KIC12 showed a
367 bloated food vacuole (Figure 4F, Figure S5D), indicating an effect on endocytosis of
368 host cell cytosol. As the effect was only partial, we decided to measure the parasite

369 and food vacuole size. This analysis with the KIC12 NLS mislocaliser parasites
370 revealed a significantly reduced food vacuole size in the parasites with inactivated
371 KIC12, while there was no effect on parasite size (Figure 4G; Figure S5 E-F). Plotting
372 the values of the individual parasites showed that the food vacuoles of similarly sized
373 parasites were consistently smaller in the KIC12 knock sideways compared to controls
374 (Figure 4H), indicating that the effect on hemoglobin delivery to the food vacuole upon
375 inactivation of KIC12 was not an indirect effect due to parasite growth impairment
376 during the assay time. Similar results were obtained using the KIC12 Lyn mislocaliser
377 line (Figure 4I-J). Quantification of the number of vesicles in trophozoites upon
378 inactivation (with either the NLS or Lyn mislocaliser) of KIC12 revealed no difference
379 to control (Figure 4K), indicating that KIC12 acted early in endocytosis, similar to the
380 previously studied K13 compartment proteins [26].
381
382 Finally, we also tested if inactivation of KIC12 by mislocalisation to the nucleus has an
383 effect on *in vitro* ART resistance, but congruent with the lacking co-localisation of
384 KIC12 with K13 in rings, RSAs showed no significantly decreased ART susceptibility
385 (Figure 4L, Figure S5G). Overall, our results indicate the presence of KIC12 at the K13
386 compartment in trophozoites, a role in HCCU and an additional pool of KIC12 in the
387 nucleus.
388
389 **Candidate proteins not detected at the K13 compartment**
390 We also generated parasites expressing endogenously C-terminally 2xFKBP-GFP-
391 2xFKBP tagged UIS14, PF3D7_1365800, PF3D7_1447800, PF3D7_0907200 and
392 VPS51 and episomally co-expressed mCherry-K13 (Figure S1H-L). Fluorescence
393 microscopy revealed no clear association with the K13 compartment in rings and
394 trophozoites in any of these parasite lines. Instead UIS14, PF3D7_1447800 and
395 VPS51 showed GFP foci within the parasite cytosol without consistent overlap with
396 mCherry-K13 foci (Figure S6A,D,F), PF3D7_0907200 showed a weak cytosolic GFP
397 signal and PF3D7_1365800 showed cytosolic GFP signal with additional foci closely
398 associated with the nucleus without consistent overlap of the main foci with mCherry-
399 K13 foci (Figure S6G and Figure S7A-B). Several attempts to generate
400 PF3D7_1243400-2xFKBP-GFP-2xFKBP^{endo} parasites remained unsuccessful,
401 indicating the gene might be refractory to C-terminal modification and hence might be
402 essential. For *vps51* and *uis14* we additionally were able to generate targeted gene
403 disruption cell lines (Figure S1M-N, Figure S6B,E), indicating these candidates are
404 dispensability for *in vitro* asexual parasite proliferation, although growth assays
405 indicated a need of UIS14 for optimal growth (Figure S6C).
406

407 Structural homology search [72] revealed the presence of a N-terminal arfaptin
408 homology (AH) domain in PF3D7_1365800 (Figure S8C), a domain known to promote
409 binding of arfaptin to Arf and Rho family GTPases important for vesicle budding at the
410 Golgi [73,74]. Given that in *Toxoplasma* an intersection of endocytosis and secretion
411 was observed at the trans Golgi [75], we tested the potential (indirect) influence of this
412 protein on endocytosis related processes. We performed conditional inactivation using
413 knock-sideways, but despite efficient loss of the PF3D7_1365800 foci no growth
414 defect was observed (Figure S7C-D) and co-expression of the Golgi marker GRASP
415 [76] revealed no consistent overlap between the foci of these two proteins (Figure
416 S7E).
417
418 Based on this analysis we did not classify UIS14, PF3D7_1365800, PF3D7_1447800,
419 PF3D7_0907200, and VPS51 as K13 compartment proteins and the location of
420 PF3D7_1243400 remains unknown.
421
422 **The domain repertoire in K13-compartment proteins**
423 With the extended complement of K13 compartment proteins from this and previous
424 work [26], we assessed the repertoire of functional domains at this site. For this we
425 took advantage of recent advances in protein structure prediction to identify structural
426 similarities in K13-compartment members for which no information could be inferred
427 from sequence homology. We compared their structures predicted with the AlphaFold
428 algorithm [72,77] with experimentally determined protein structures in the Protein Data
429 Bank and identified 25 domains, 15 of which were not previously identified according
430 to PlasmoDB and Interpro (Figure 5A,B and S8).
431
432 The largest number of recognisable folds were detected in KIC4, a protein for which
433 we previously detected some similarity to α-adaptins [26]. KIC4 contained an N-
434 terminal VHS domain (IPR002014), followed by a GAT domain (IPR004152) and an
435 Ig-like clathrin adaptor α/β/γ adaptin appendage domain (IPR008152) (Figure 5A-C,
436 Figure S8). This is an arrangement typical for GGAs (Golgi-localised gamma ear-
437 containing Arf-binding proteins) which are vesicle adaptors first found to function at
438 the trans-Golgi [78,79]. Surprisingly, KIC4 however also contains an additional domain
439 at its C-terminus, a β-adaptin appendage C-terminal subdomain (IPR015151) which
440 is a part of the ear domain of β-adaptins and not found in GGAs. Together with the
441 preceding clathrin adaptor α/β/γ adaptin domain, the C-terminus of KIC4 therefore
442 resembles a β-adaptin. The region without detectable fold after the GAT domain likely
443 corresponds to the hinge region in GGAs. This suggests that KIC4 is a hybrid between
444 GGAs and an AP complex subunit beta (Figure 5C), the two known types of adaptors.

445 Based on Interpro [80], such a domain organization has to date not been observed in
446 any other protein.
447
448 KIC5 also contains a clathrin adaptor α/β/γ-adaptin domain (IPR008152) and one of
449 the two subdomains of the ear domain of α-adaptins (clathrin adaptor α-
450 adaptin_appendage C-terminal subdomain, IPR003164) (Figure 5 A,B,D). More than
451 97% of proteins containing these domains also contain an Adaptin_N (IPR002553)
452 domain and function in vesicle adaptor complexes as subunit α (Figure 5D) but no
453 such domain was detectable in KIC5. KIC5 thus displays some similarities to AP
454 complex subunit α but similar to KIC4, there appear to be profound difference to the
455 canonical adaptors.
456
457 KIC7 contains an ArfGAP domain, as recently also predicted for its *Toxoplasma*
458 homolog AGFG (TGME49_257070) [81]. ArfGAPs regulate the activity of Arfs which
459 are small GTP binding proteins coordinating vesicle trafficking [82,83]. UBP1 contains
460 a ubiquitin specific protease (USP) domain at its C-terminus which previously led to
461 its name ubiquitin carboxyl-terminal hydrolase 1 (UBP1) [84]. Here we also identified
462 a VHS domain in its centre. VHS domains occur in vesicular trafficking proteins,
463 particularly in endocytosis proteins, but typically are found at the N-terminus of
464 proteins (in over 99.8% of cases according to annotations by Interpro). A combination
465 with a USP domain has not been observed so far. If the VHS domain is functional in
466 UBP1 despite its central position, it is the first structural domain that would support the
467 functional data [26] showing this K13 compartment protein has a role in endocytosis.
468
469 In KIC12 we identified a potential purple acid phosphatase (PAP) domain. However,
470 with the high RMSD of 4.9 Å, the domain might also be a divergent similar fold, such
471 as a C2 domain, which targets proteins to membranes. KIC2 contains a GAR domain
472 which typically bind the cytoskeleton [85] and KIC3 contains a PAH domain which can
473 serve as a scaffold for transcription factors [86,87]. While not consistently detected at
474 the K13 compartment, it is interesting that we here found that PF3D7_1365800
475 contains an AH domain, a member of the AH/BAR domain family (Figure S8C).
476 According to Interpro, no AH or BAR domain proteins have so far been detected in
477 malaria parasites, rendering this an interesting protein. However, as we here found it
478 to be likely dispensable for intra-erythrocytic parasite development and in light of no
479 strong indication for the presence in regions containing K13, it seems to be of little
480 relevance for endocytosis.
481
482 Overall this analysis revealed that most of the proteins involved in endocytosis or *in*
483 *vitro* ART resistance contain regions with structural homology to vesicle trafficking

484 domains, often specific for endocytosis (Figure 6E). However, apart from AP2 the
485 domain arrangements are unusual, the conservation on the primary sequence level is
486 low (which precluded initial detection) and there are large regions without any
487 resemblance to other proteins, altogether indicating strong parasite-specific
488 adaptations. In contrast, the K13 compartment proteins where no role in ART
489 resistance (based on RSA) or endocytosis was detected, such as KIC2 or KIC11, do
490 not contain such domains (Figure 6E). This analysis suggests that proteins detected
491 at the K13 compartment can be classified into at least two groups of which one is
492 involved in endocytosis and *in vitro* ART resistance whereas the other might have
493 different functions yet to be discovered.
494
495 **DISCUSSION**
496 The BioID proxiome of K13 and Eps15 revealed the first proteins involved in the initial
497 steps of endocytosis in malaria parasites, a process that in blood stage parasites leads
498 to the uptake of large quantities of host cell cytosol. As demonstrated in model
499 organisms, endocytosis is a complex and highly regulated process involving a
500 multitude of proteins [88–90], but in Apicomplexan parasites is not well studied [33].
501 Thus, the K13 compartment proxiome represents an opportunity to identify proteins
502 involved in this process in malaria parasites and will be important to understand it on
503 a mechanistic level. Understanding how and if HCCU differs from the canonical
504 endocytic processes in human cells, will not only help to understand this critical
505 process in parasite biology but might also reveal parasite-specific aspects that permit
506 specific inhibition and could be targets for drug development efforts.
507
508 Here we expanded the repertoire of K13 compartment proteins and functionally
509 analysed several of them. An assessment of structural similarities indicated an
510 abundance of vesicle trafficking - and more specifically - endocytosis domains, in the
511 confirmed K13 compartment proteins. The proteins with such domains now comprise
512 KIC4, KIC5, KIC7, Eps15, AP2μ and UBP1, all of which reduce *in vitro* ART
513 susceptibility when inactivated, indicating that this led to a reduced endocytosis in ring
514 stages [26]. A role in endocytosis has been experimentally shown for all of these
515 except for KIC4 and KIC5, for which only gene disruptions are available which are less
516 suitable for endocytosis assays [26].
517
518 Besides the AP2 complex, the structural similarity analysis indicated that two
519 additional K13 compartment proteins (KIC4 and KIC5) contain domains found in
520 adaptor subunits. KIC4 and KIC5 likely have additional rather than redundant roles to
521 the AP2 complex, as the AP2 complex is essential for blood stage growth and on its
522 own needed for HCCU [26,91]. While KIC4 disruption did not lead to a growth defect,

523 disruption of KIC5 impaired parasite growth [26], indicating that there cannot be full
524 redundancy between these two proteins either. Altogether these considerations
525 support specific individual roles of all the known K13 compartment proteins with
526 adaptor domains.
527
528 In model organisms, the α/β/γ-adaptin appendage domain, the α-adaptin domain and
529 the β-adaptin domain, in the AP2 complex and/or in GGAs, act as interaction hubs for
530 more than 15 accessory proteins, including Eps15, Arfs, amphiphysin, epsins and
531 rabaptins as well as lipids involved in vesicle budding [92]. This fits with the presence
532 of Eps15 and KIC7 (which contains an ArfGAP domain) at the K13 compartment. The
533 interaction between the α/β/γ-adaptin appendage domain and Eps15 has been
534 captured by X-ray crystallography (2I9V) [92], highlighting a possible functional
535 connection between Eps15 and AP-2α, AP-2β, KIC4 or KIC5, which all contain this
536 domain. Indeed, the *Toxoplasma* homologue of KIC4 has recently been shown to bind
537 Eps15, while *Tg*AP-2α did not [81].
538
539 Despite the detection of various domains in K13 compartment proteins it is noteworthy
540 that most of these proteins (e.g. EPS15, UBP1, KIC7) still contain large regions without
541 any homology to other proteins. The parasite-specific nature of the initial steps of
542 endocytosis is also evident from the difficulty of primary sequence-based detection of
543 the vesicular trafficking domains in K13 compartment proteins and from the unusual
544 domain combinations. Furthermore it is peculiar that despite the presence of the
545 clathrin adaptor AP2, clathrin itself does not seem to be involved [26,91], further
546 indicating parasite-specific features of HCCU. Overall, this indicates a strongly
547 adapted mechanism of the first steps in endocytosis for HCCU in malaria parasites.
548 One protein typically involved in endocytosis that did not appear in the list of highly
549 enriched proteins of the K13 and Eps15 proxiome is a dynamin [93] which might
550 indicate further differences to the canonical mechanism in model organism. However,
551 at least in *Toxoplasma* an association of K13 and its compartment with a dynamin was
552 reported [81,94], indicating that an equivalent is likely also present in malaria
553 parasites.
554
555 A protein that has a more canonical structure is MyoF, a Class XXII myosin [95], which
556 we here link with endocytosis and found in foci that were often close or overlapping
557 with the K13 compartment. The only partial overlap could indicate that either it i) only
558 transiently associates with the K13 compartment, or ii) is in a separate compartment
559 that is close to the K13 compartment or iii) is in a region of the K13 compartment that
560 is close, but non-overlapping, with that defined by the other K13 compartment proteins.
561 A number of conclusions can be drawn from our MyoF characterisation. Firstly, its

562 inactivation resulted in the appearance of vesicles, similar to the phenotype of VPS45
563 inactivation [44], indicating it has a role in endosomal transport, downstream of the
564 initial steps of endocytosis. This is in contrast to the other K13 compartment proteins
565 and might explain the only partial overlap in location of MyoF with the K13
566 compartment. Secondly, its involvement suggests a role of actin/myosin in endosomal
567 transport which is well known from other organisms [96,97] and supports the
568 observation that the actin inhibitor CytochalasinD leads to vesicles similar to MyoF
569 inactivation [39,43]. Hence, myosin may generate force needed for the transport of
570 host cell cytosol filled vesicles to the food vacuole. Thirdly, there was no effect of MyoF
571 inactivation on ART resistance, which might indicate that there is no need for
572 actin/myosin for endocytosis in rings. Although there were some limitations to our
573 system to study MyoF, the substantial inactivation caused by simply tagging MyoF
574 would already have led to a decreased susceptibility to ART in RSAs (as seen with
575 other K13 compartment proteins [26]), if ring stage endocytosis had been affected,
576 which was not the case. It is of note that the endocytosis function of MyoF is reciprocal
577 to that of K13 which is only required in rings, indicating that there appear to be stage-
578 specific differences in endocytosis between these stages. However, the majority of
579 components are at the K13 compartment throughout the cycle and for instance KIC7
580 is needed for HCCU in both rings and trophozoites [26].
581
582 Attempts to generate a knockout of *P. berghei myof* were reported to be unsuccessful
583 [95], while a genome-wide mutagenesis screen predicted *Pf*MyoF to be dispensable
584 for asexual blood stage development [98]. *Tg*MyoF has been previously implicated in
585 Golgi and rhoptry positioning [99] or centrosomes positioning and apicoplast
586 inheritance [100]. We cannot exclude that beside the effect on HCCU, a part of the
587 growth defect we see after MyoF inactivation arises from similar functions in blood
588 stages.
589
590 MCA2 has been identified as putative K13 interaction candidate, but its location was
591 unknown [26]. Here, we establish MCA2 as member of the K13 compartment by
592 endogenously tagging it with HA as well as by using a cell line with a truncated MCA2
593 fused to GFP. MCA2 was located in foci overlapping with the K13 compartment and
594 in schizonts the foci were in proximity of the IMC in line with previous data linking the
595 K13 compartment and the IMC [54]. A close association of the K13 compartment and
596 the IMC is also supported by recent work in *T. gondii* showing that the K13
597 compartment and its proteins are present at the IMC embedded micropore [81].
598
599 We previously showed that gene disruption of *mca2* results in reduced *in vitro* parasite
600 proliferation and *in vitro* ART resistance [26], which is also supported by a knockout of

601 the *mca2* homologue in the rodent infecting *P. berghei* [101,102]. Truncation of MCA2
602 at amino acid position Y1344 still resulted in decreased ART susceptibility, even
603 though the susceptibility reduction was less than a disruption at amino acid position
604 57. In contrast to the full disruption, truncation at residue 1344 did not lead to a growth
605 defect, indicating that the predicted metacaspase domain (AA 1527-1848) – not
606 present in this truncated MCA2 protein – is dispensable for asexual parasite
607 proliferation. This finding is in contrast to results indicating an important role of the
608 metacaspase domain for parasite proliferation using MCA2 inhibitors [103–105].
609
610 Here we also identified the first protein, KIC11, at the K13 compartment that had an
611 important function for the growth of blood stage parasites but did not appear to function
612 in endocytosis. Instead, KIC11 had an important function in late-stage parasites.
613 KIC11 was predicted to be non-essential by a genome-wide mutagenesis screen [98],
614 while the orthologue in the rodent malaria parasite *P. berghei* (PBANKA_0906900)
615 was classified as essential for asexual proliferation in the PlasmoGem screen [106].
616
617 Overall the classification of K13 compartment proteins presented in this work indicates
618 that there are two main groups. The first group comprises proteins that define a highly
619 unusual endocytic pathway to internalise host cell cytosol. These proteins are
620 predominately parasite-specific (exceptions being AP2μ, MyoF and in part K13 which
621 however lacks vesicle trafficking domains). This group can be further categorised into
622 a larger subgroup that is involved in *in vitro* ART resistance and a smaller subgroup,
623 such as KIC12 and MyoF that do not confer *in vitro* ART resistance when inactivated,
624 presumably because they are not needed for endocytosis in rings. In the case of MyoF
625 this idea is supported by low expression in rings whereas KIC12 was not at the K13
626 compartment in rings. Reciprocal to this, we found in previous work that K13 is needed
627 for endocytosis in ring stages only [26]. Hence, there is heterogeneity in the stage-
628 specificity of the endocytosis proteins at the K13 compartment. In terms of function,
629 most of the endocytosis and *in vitro* ART resistance group of K13 compartment
630 proteins are involved in the initial phase of HCCU. In contrast to VPS45 [44] their
631 inactivation does not result in the generation of endosomal intermediates in the
632 parasite cytoplasm. The exception is MyoF which (of the proteins here classified as
633 K13 compartment associated) generated vesicles when inactivated. MyoF showed the
634 lowest spatial overlap with K13 and may form a link to downstream steps of endosomal
635 transport. The second group of K13 compartment proteins has no role in endocytosis
636 or *in vitro* ART resistance and do not contain vesicle trafficking domains (as based on
637 our domain identification here). They likely serve other functions but the homogeneity
638 of functions of this group is unclear. KIC11, the first essential protein of this group,
639 might help to shed light on the function of the non-endocytosis related K13

640 compartment proteins. However, it should be noted that KIC11 showed only partial
641 overlap with the K13 compartment in schizonts, the stage relevant for the observed
642 phenotype of the inactivation of this protein. Hence, it is possible that KIC11's essential
643 function is not at the K13 compartment. Overall, this work strengthens the notion that
644 the K13 compartment is involved in endocytosis, reveals novel essential HCCU
645 proteins and provides a classification of its members that might inform future studies
646 to understand the unusual mechanism of endocytosis in apicomplexans.
647
648 **METHODS**
649 ***P. falciparum* culture**
650 Blood stages of *P. falciparum* 3D7 [107] were cultured in human red blood cells (O+ ;
651 University Medical Center Hamburg, Eppendorf (UKE)). Cultures were maintained at
652 37°C in an atmosphere of 1 % O_2, 5 % CO_2 and 94 % N_2 using RPMI complete medium
653 containing 0.5 % Albumax according to standard protocols [108].
654 In order to obtain highly synchronous parasite cultures, late schizonts were isolated
655 by percoll gradient [109] and cultured with fresh erythrocytes for 4 hours. Afterwards
656 sorbitol synchronization [110] was applied in order to remove remaining schizonts
657 resulting in a highly synchronous ring stage parasite culture with a four-hour age
658 window.
659
660 **Cloning of plasmid constructs for parasite transfection**
661 For endogenous C-terminal 2x-FKBP-GFP-2xFKBP tagging using the SLI system [63]
662 a homology region of 321-1044 bp (1044 bp for *Pfmyof* (PF3D7_1329100), 690 bp for
663 *Pfkic11* (PF3D7_1142100), 780 bp for PF3D7_1447800, 695 bp for *Pfkic12*
664 (PF3D7_1329500), 411 bp for PF3D7_1243400, 321 bp for PF3D7_1365800, 674 bp
665 for *Pfuis14* (PF3D7_0405700), 698 bp for PF3D7_0907200, 756 bp for *Pfvps51*
666 (PF3D7_0103100)) was amplified from 3D7 gDNA and cloned into pSLI-sandwich [63]
667 using the NotI/MluI restriction site.
668 For endogenous C-terminal 2x-FKBP-GFP tagging using the SLI system [63] a
669 homology region of 1044 bp for *Pfmyof* (PF3D7_1329100), was amplified using 3D7
670 gDNA and cloned into pSLI-2xFKBP-GFP [63] using the NotI/MluI restriction site.
671 For endogenous C-terminal 3xHA tagging using the SLI system [63] a homology
672 region of 948-999 bp (999 bp for *Pfmca2* (PF3D7_1438400), 948 bp for *Pfmyof*
673 (PF3D7_1329100)) was amplified using 3D7 gDNA and cloned into pSLI-3xHA [111]
674 using the NotI/XhoI restriction site.
675 For generating *Pf*MCA2^{Y1344Stop}-GFP a 984 bp homology region was amplified using
676 3D7 gDNA and cloned into the pSLI-TGD plasmid [63] using NotI and MluI restriction
677 sites.

678 For targeted gene disruption (TGD) a 429-617 bp (534 bp for *kic12* (PF3D7_1329500),
679 615 bp for *Pfkic11* (PF3D7_1142100), 617 bp for *Pfuis14* (PF3D7_0405700), 429 bp
680 for *Pfvps51* (PF3D7_0103100)) was amplified using 3D7 gDNA and cloned into the
681 pSLI-TGD plasmid [63] using NotI and MluI restriction sites.
682 All oligonucleotides used to generate DNA fragments as well as those used for
683 genotyping PCRs are listed in table S2.
684 For co-localisation experiments the plasmids p40PX-mCherry [44], pmCherry-
685 K13_DHODH^{nmd3} [26], ^{ama1}PhIL1mCherry [112] and pGRASPmCherry-BSD^{nmd3} [26]
686 were used.
687
688 **Transfection of *P. falciparum***
689 For transfection, Percoll-purified [109] parasites at late schizont stage were
690 transfected with 50 µg plasmid DNA using Amaxa Nucleofector 2b (Lonza,
691 Switzerland) as previously described [113]. Transfectants were selected using either
692 4 nM WR99210 (Jacobus Pharmaceuticals), 0.9 µM DSM1 [114] (BEI Resources) or
693 2 mg/ml for Blasticidin (BSD) (Invitrogen). In order to select for parasites carrying the
694 genomic modification via the SLI system [63], G418 (ThermoFisher, USA) at a final
695 concentration of 400 µg/mL was added to a culture with about 5 % parasitemia. The
696 selection process and integration test were performed as previously described [63].
697
698 **Imaging**
699 All fluorescence images were captured using a Zeiss Axioskop 2plus microscope with
700 a Hamamatsu Digital camera (Model C4742-95) or for confocal imaging an Olympus
701 FluoView 1000 confocal microscope.
702 Microscopy of live parasite-infected erythrocytes was performed as previously
703 described [115]. Approximately 5 µL of infected erythrocytes were added on a glass
704 slide and covered with a cover slip. Nuclei were stained with 1 µg/mL Hoechst-33342
705 (Invitrogen) or 1µg/mL 4',6'-diamidine-2'-phenylindole dihydrochloride (DAPI)
706 (Roche).
707 Immunofluorescence assays (IFA) were performed as previously described [111].
708 Asynchronous parasite cultures with 5% parasitemia were harvested, washed twice
709 with PBS, air-dried as thin monolayers on 10-well slides (Thermo Fischer) and fixed in
710 100% acetone for 30 min at room temperature. After rehydration with PBS, the cells
711 were incubated with primary antibody solution containing rabbit a-HA (1:500) (Cell
712 Signalling) and rat a-RFP (1:500) (Chromotek) diluted in 3% BSA in PBS. After three
713 wash steps with PBS, incubation with corresponding secondary antibodies (Molecular
714 probes) was performed. Slides were sealed with a coverslip using mounting medium
715 (Dako).
716

717 **Parasite proliferation assay**
718 For proliferation assays a flow cytometry based assay, adapted from previously
719 published assays [44,116], was performed to measure multiplication over five days.
720 For knock sideways experiments, the same culture was split into control and + 250 nM
721 rapalog at the start of the proliferation assay and growth of each of these two cultures
722 followed over the course of the assay. Each day parasite cultures were resuspended
723 and 20 µL samples were transferred to an Eppendorf tube. 80 µL RPMI containing
724 Hoechst-33342 and dihydroethidium (DHE) was added to obtain final concentrations
725 of 5 µg/mL and 4.5 µg/mL, respectively. Samples were incubated for 20 min (protected
726 from UV light) at room temperature, and parasitemia was determined using an LSRII
727 flow cytometer by counting 100,000 events using the FACSDiva software (BD
728 Biosciences).
729
730 **Immunoblotting**
731 Protein samples were resolved by SDS-PAGE and transferred to Amersham Protran
732 membranes (GE Healthcare) in a tankblot device (Bio-Rad) using transfer buffer
733 (0.192 M Glycine, 0.1% SDS, 25 mM Tris) with 20% methanol. Next, membranes were
734 blocked for 30 minutes with 5% skim milk, and incubated with primary antibodies
735 diluted in PBS containing 5% skim milk for 2h or overnight, followed by three washing
736 steps with PBS and 2h incubation with horseradish peroxidase-conjugated secondary
737 antibodies diluted in PBS containing 5% skim milk. Detection was perfomed using the
738 Clarity Western ECL kit (Bio-Rad), and signals were recorded with a ChemiDoc XRS
739 imaging system (Bio-Rad) equipped with Image Lab software 5.2 (Bio-Rad).
740 Antibodies were applied in the following dilutions: mouse a-GFP (1:1000) (Roche), rat
741 a-HA (1:2000) (Roche), rabbit anti-aldolase (1.2000) [117], goat α-rat (1:2000)
742 (Dianova), goat α-mouse (1:2000) (Dianova) and donkey α-rabbit (1:2000) (Dianova).
743
744 **Conditional inactivation via knock-sideways**
745 For knock-sideways cell lines were transfected with plasmids encoding the nuclear
746 mislocaliser (NLS-FRB-mCherry) ot the PPM mislocaliser (Lyn-FRB-mCherry) [63].
747 The knock-sideways approach was performed as described previously [63]. Briefly,
748 cultures were split into two 2-ml cultures of which one was supplemented with 250 nM
749 rapalog (Clontech). Mislocalisation of the target protein was verified by live-cell
750 microscopy.
751
752 **Ring stage survival assay (RSA)**
753 RSAs were done as described previously [23,26]. Schizonts were purified from an
754 asynchronous parasite culture using a percoll gradient [109] and were allowed to
755 invade fresh RBCs at 37°C for 3 hours after which they were synchronised with 5%

756 sorbitol [110] to obtain 0 - 3 hour old rings. These rings were washed 3 times with
757 medium and challenged with 700 nM DHA for 6 hours. Afterwards, the cells were
758 washed three times in RPMI medium and the parasites were grown for another 66
759 hours. Finally, Giemsa smears were prepared in order to determine the parasite
760 survival rate (parasitemia of viable parasites after DHA compared to parasitemia of
761 non-DHA treated control). 1% parasite survival rate was considered the threshold for
762 *in vitro* ART resistance [23]. Number of cells counted are indicated in the
763 corresponding Figure legends.
764
765 **Vesicle accumulation assay**
766 The vesicle accumulation assay was adapted from [44]. Briefly, the number of vesicles
767 per parasite were determined based on DIC images of synchronised trophozoites. For
768 this, parasite cultures were two times synchronised (6-8 hours apart) using 5% sorbitol
769 [110], split into two 2ml dishes of which one received rapalog to a final concentration
770 of 250 nM, while the other culture served as control without rapalog and then grown
771 for 16-24 hours to obtain trophozoite stages. Parasites were imaged in the DIC
772 channel and the vesicles in the DIC images were counted. The assay was performed
773 blinded and in at least three independent experiments (n of analysed cells indicated in
774 the corresponding Figure legend).
775
776 **Bloated food vacuole assay / E64 hemoglobin uptake assay**
777 The bloated food vacuole assay was performed as previously described [44]. Briefly,
778 ring stage parasite cultures with an 8h time window were obtained using double 5%
779 sorbitol synchronisation. Parasites were either split into two 2ml dishes of which one
780 received rapalog to a final concentration of 250 nM, while the other culture served as
781 control without rapalog for *Pf*KIC11 and *Pf*KIC12 (see experimental setup scheme in
782 Figure S4C, S5D) and incubated at 37°C overnight, or first incubated at 37°C overnight
783 and split at the start of the assay for *Pf*MyoF (see experimental setup scheme in Figure
784 S3E). When parasites reached the young trophozoites stage, the medium was
785 aspirated and 1 ml medium containing 33 mM E64 protease inhibitor (Sigma Aldrich)
786 was added. The cells were cultured for 8 hours and then imaged. The DIC image was
787 used for scoring bloated food vacuoles and determination of parasite and food vacuole
788 size. For visualisation of bloated food vacuoles, the cells were stained with 4.5 mg/ml
789 dihydroethidium (DHE) for 15 minutes at 37°C. The experiment was performed blinded
790 and in three independent experiments.
791
792 **Domain identification using AlphaFold.**
793 The predicted protein structures of all known K13-compartment members were
794 downloaded from the AlphaFold Protein Structure Database (alphafold.ebi.ac.uk) [72],

except for UBP1 which was not available. The structure for UBP1 was predicted in 6 parts, coving resides 1-640, 641-1280, 1281-1920, 1921-2560, 2561-2880 and 2881-3499 using ColabFold [118]. VAST searches (ncbi.nlm.nih.gov/Structure/VAST/vastsearch.html) [119] were performed on all structures. The top 3 hits for each protein and protein part where aligned with the search model using the PyMol command cealign (Schrödinger, USA). Similarities with RMSDs of under 5 Å over more than 60 amino acids are listed in the results. Domains that were not previously annotated in Interpro (as of April 2022) [80] or PlasmoDB v.57 [120] were considered as newly identified.

Software

Statistical analyses were performed with GraphPad Prism version 8 (GraphPad Software, USA), microscopy images were processed in Corel Photo-Paint X6-X8 (https://www.coreldraw.com) or Fiji [121], plasmids and oligonucleotides were designed using ApE [122]. Protein structures were analysed and visualized using PyMol (Schrödinger, USA). Figures were arranged in CorelDraw X6-8.

Acknowledgements

We thank Jacobus Pharmaceuticals for WR99210. DSM1 (MRA-1161) was obtained from MR4/BEI Resources, NIAID, NIH. We thank Tim Gilberger for providing the PhIL1mcherry plasmid.

Author contribution

Conceptualization: TS
Validation: CCP
Formal Analysis: JSWM, SS, HB, TS
Investigation: JSWM, SS, HB, JB, IH, EJ, SS, SF
Resources: JB, EJ, SF, TS
Writing – original Draft: JSWM, HB, TS
Writing – Review & Editing: JSWM, HB, IH, TS
Visualization: JSWM, SS, HB, IH, TS
Supervision: TS
Funding Acquisition: TS
All authors read and approved the manuscript.

Funding

HMB acknowledges funding by the Ortrud Mührer Fellowship of the Vereinigung der Freunde des Tropeninstituts Hamburg e.V, CCP thanks DAAD for funding. This work was funded by the European Research Council (ERC, grant 101021493).

834
835
836 **Figures:**
837
838 **Table 1: Selection of putative K13 compartment proteins for further**
839 **characterization in this manuscript**
840
841 **Figure 1: MCA2 is part of the K13 compartment and its truncation reduces ART**
842 **susceptibility**
843 **(A)** Schematic representation and nomenclature of MCA2 fusion proteins (not to scale)
844 expressed in the parasite by modification of the endogenous gene. GFP in green,
845 3xHA in red and metacaspsase domain in grey. Amino acid positions are indicated by
846 numbers. **(B)** Localisation of MCA2^{Y1344STOP}-GFP by live-cell microscopy across the
847 intra-erythrocytic development cycle. Nuclei were stained with DAPI. Scale bar, 5 µm.
848 (**C)** Live cell microscopy images of parasites expressing the truncated MCA2^{Y1344STOP}-
849 GFP fusion protein with an episomally expressed mCherry-K13 fusion protein. Foci
850 were categorized into 'overlap' (black), 'partial overlap' (dark grey) and 'no overlap'
851 (light grey) and shown as frequencies in the pie chart (n = 46 cells were scored from
852 a total of three independent experiments). **(D)** Live cell microscopy images of parasites
853 expressing the truncated MCA2^{Y1344STOP}-GFP fusion protein with the IMC marker
854 protein PhIL1mCherry. Zoom, enlarged region (factor 400%). **(E)** Relative growth of
855 MCA2^{Y1344STOP} compared with 3D7 wild type parasites after two growth cycles. Each
856 dot shows one of four independent experiments. P-values determined by one-sample
857 t-test. **(F)** Parasite survival rate (% survival compared with control without DHA) 66 h
858 after 6 h DHA treatment in standard RSA. Two (3D7) or three (MCA2 ^{Y1344STOP})
859 independent experiments, p-value determined by unpaired t-test. Green dashed line
860 indicates 1% ART resistance cut-off [23]; 3419-3828 (mean 3632) erythrocytes for
861 control and 10364-11734 (mean 11254) cells for DHA treated samples were counted.
862 Nuclei were stained with DAPI (B) or Hoechst-33342 (D); scale bars, 5 µm and for
863 zoom 1 µm.
864
865 **Figure 2: MyoF is involved in host cell cytosol uptake and associated with the**
866 **K13 compartment**
867 **(A)** Localisation of MyoF-2xFKBP-GFP-2xFKBP expressed from the endogenous
868 locus by live-cell microscopy across the intra-erythrocytic development cycle. Nuclei
869 were stained with DAPI. **(B)** Live cell microscopy images of parasites expressing the
870 MyoF-2xFKBP-GFP-2xFKBP fusion protein with an episomally expressed FV marker
871 P40PX-mCherry. **(C)** Live cell microscopy images of parasites expressing the MyoF-
872 2xFKBP-GFP-2xFKBP fusion protein with episomally expressed mCherry-K13. Foci

873 were categorized into ‘overlap’ (black), ‘partial overlap’ (dark grey), ‘close foci’ (=less
874 than one focus radius apart) (light blue) and ‘non overlap’ (light grey). Three
875 independent live microscopy sessions with each n=14 analysed parasites. **(D)** Relative
876 growth of MyoF-2xFKBP-GFP-2xFKBP^{endo} compared with 3D7 wild type parasites
877 after two growth cycles. Each dot shows one of four independent growth experiments.
878 P-values determined by one-sample t-test. **(E)** Live-cell microscopy of knock sideways
879 (rapalog) and control MyoF-2xFKBP-GFP-2xFKBP^{endo}+1xNLSmislocaliser parasites 1
880 hour or 22 hours after the induction by addition of rapalog. **(F)** Relative growth of 3D7
881 and MyoF-2xFKBP-GFP-2xFKBP^{endo}+1xNLSmislocaliser parasites (+ rapalog)
882 compared with the corresponding control parasites (without rapalog) after two growth
883 cycles. Three (3D7) and eight (MyoF-2xFKBP-GFP-2xFKBP^{endo}) independent
884 experiments (individual experiments shown in Figure S3D). Error bars, mean ± SD. P-
885 values determined by Welch’s t-test. **(G)** Number of vesicles per parasite in
886 trophozoites determined by live-cell fluorescence microscopy (DIC) in 3D7 and MyoF-
887 2xFKBP-GFP-2xFKBP^{endo}+1xNLSmislocaliser parasites with and without rapalog
888 addition. Three (3D7) and six (MyoF-2xFKBP-GFP-2xFKBP^{endo}+1xNLSmislocaliser)
889 independent experiments with each time n=16-25 (mean 20.9) parasites analysed per
890 condition. Mean of each independent experiment indicated by coloured triangle,
891 individual datapoints by grey dots. Data presented according to SuperPlot guidelines
892 [123]; Error bars represent mean ± SD. P-value for ± rapalog determined by paired t-
893 test and for 3D7 vs MyoF by Mann-Whitney. Representative DIC images are
894 displayed. **(H)** Bloated food vacuole assay with MyoF-2xFKBP-GFP-2xFKBP^{endo}
895 parasites 8 hours after inactivation of MyoF (+ rapalog) compared with controls (-
896 rapalog). Cells were categorized as with ‘bloated FV’ or ‘non-bloated FV’ and
897 percentage of cells with bloated FV is displayed; n = 4 independent experiments with
898 each n=33-40 (mean 34.6) parasites analysed per condition. P-values determined by
899 Welch’s t-test. Representative DIC and fluorescence microscopy images shown on
900 the right. Parasite cytoplasm was visualized with DHE. Experimental setup shown in
901 Figure S3E. **(I)** Parasite survival rate (% survival compared to control without DHA) 66
902 h after 6 h DHA (700 nM) treatment in standard RSA. MyoF-2xFKBP-GFP-2xFKBP^{endo}
903 parasites + 1xNLSmislocaliser were pre-treated with rapalog either 12 or 24 hours
904 prior to the assay. Three independent experiments, P-value determined by Wilcoxon
905 test. Green dashed line indicates 1% ART resistance cut-off [23]. 2988-8392 (mean
906 5102) cells for control and 22704-44038 (mean 32077) cells for DHA treated samples
907 were counted. Experimental setup shown in Figure S3F. Scale bars, 5 µm.
908
909 **Figure 3: KIC11 is a K13 compartment protein important for asexual parasite**
910 **proliferation, but not involved in endocytosis or *in vitro* ART resistance**

(A) Localisation of KIC11-2xFKBP-GFP-2xFKBP expressed from the endogenous locus by live-cell microscopy across the intra-erythrocytic development cycle. (**B)** Live cell microscopy images of parasites expressing KIC11-2xFKBP-GFP-2xFKBP with episomally expressed mCherry-K13. White arrowheads indicate overlapping foci. Nuclei were stained with DAPI. Scale bar, 5 µm. **(C)** Live-cell microscopy of knock sideways (+ rapalog) and control (without rapalog) KIC11-2xFKBP-GFP-2xFKBP^{endo}+1xNLSmislocaliser parasites 4 and 16 hours after the induction of knock-sideways by addition of rapalog. Scale bar, 5 µm. **(D)** Relative growth of KIC11-2xFKBP-GFP-2xFKBP^{endo}+1xNLSmislocaliser (blue) and KIC11-2xFKBP-GFP-2xFKBP^{endo}+ LYNmislocaliser (red) plus rapalog compared with control parasites over two growth cycles. Five independent experiments were performed (depicted by different symbols) and mean relative parasitemia ± SD is shown (individual experiments shown in Figure S4A). **(E)** Parasite stage distribution in Giemsa smears at the time points (average hours post invasion, h) indicated above each bar in tightly synchronised (±4h) KIC11-2xFKBP-GFP-2xFKBP^{endo}+1xNLSmislocaliser parasites (rapalog addition at 4 hpi, 20 hpi, or 32 hpi and control) assayed over two consecutive cycles (last time point in cycle 3). A second replicate is shown in Figure S4B. **(F)** Giemsa smears of control and at 4 hpi, 20 hpi, or 32 hpi rapalog-treated KIC11-2xFKBP-GFP-2xFKBP^{endo}+1xNLSmislocaliser parasites shown in (E). **(G)** Number of vesicles per parasite in trophozoites determined by live-cell fluorescence microscopy (DIC) in KIC11-2xFKBP-GFP-2xFKBP^{endo}+1xNLSmislocaliser parasites with and without rapalog. Four independent experiments with n=16-59 (mean 30.1) parasites analysed per condition per experiment. Mean of each independent experiment indicated by coloured triangle, individual datapoints by grey dots. Data presented according to SuperPlot guidelines [123]; Error bars represent mean ± SD. P-value determined by paired t-test. Representative DIC images are displayed. **(H)** Bloated food vacuole assay with KIC11-2xFKBP-GFP-2xFKBP^{endo} parasites 8 hours after inactivation of KIC11 (+rapalog) compared with control (without rapalog). Cells were categorized as with ‘bloated FV’ or ‘non-bloated FV’ and displayed as percentage of cells with bloated FV; n=3 independent experiments with each n=19-36 (mean 26.5) parasites analysed per condition. P-values determined by Welch’s t-test. Representative DIC and fluorescence microscopy images are shown in the right panel. Parasite cytoplasm was visualized with DHE. Experimental setup shown in Figure S4C. **(I)** Parasite survival rate (% survival compared to control without DHA) 66 h after 6 h DHA treatment in standard RSA. Three independent experiments, P-value determined by paired t-test. Green dashed line indicates 1% ART resistance cut-off [23]. 2896-7135 (mean 4502) cells for control and 23183-32455 (mean 28496) cells for DHA treated samples were counted. Experimental setup shown in Figure S4D. Nuclei were stained with DAPI (A, B). Scale bars, 5 µm.

950

951 **Figure 4: KIC12 shows a dual localisation in the nucleus and at the K13**
952 **compartment and is involved in endocytosis but not in ART resistance**
953 **(A)** Localisation of KIC12-2xFKBP-GFP-2xFKBP expressed from the endogenous
954 locus by live-cell microscopy across the intra-erythrocytic development cycle. Arrow
955 heads indicate foci (white) and nuclear (light blue) signal. (**B)** Live cell microscopy
956 images of parasites expressing KIC12-2xFKBP-GFP-2xFKBP with episomally
957 expressed mCherry-K13. Black arrowheads indicate overlapping foci. Nuclei were
958 stained with DAPI. Scale bar, 5 µm. Extended panel shown in Figure S5A. **(C)** Live-
959 cell microscopy of knock sideways (+ rapalog) and control (without rapalog) KIC12-
960 2xFKBP-GFP-2xFKBP^{endo}+1xNLSmislocaliser parasites 4 and 16 hours after the
961 induction of knock-sideways by addition of rapalog. **(D)** Relative growth of KIC12-
962 2xFKBP-GFP-2xFKBP^{endo}+1xNLSmislocaliser (blue) and KIC12-2xFKBP-GFP-
963 2xFKBP^{endo}+Lyn-mislocaliser (red) parasites plus rapalog compared with the
964 corresponding untreated control parasites over two growth cycles. Five independent
965 growth experiments were performed and mean relative parasitemia +/- SD is shown
966 (all replicas shown in Figure S5B and C). **(E)** Live-cell microscopy of knock sideways
967 (+ rapalog) and control (without rapalog) KIC12-2xFKBP-GFP-2xFKBP^{endo}+Lyn-
968 mislocaliser parasites 4 hours after the induction of knock-sideways by addition of
969 rapalog. **(F)** Bloated food vacuole assay with KIC12-2xFKBP-GFP-2xFKBP^{endo}
970 parasites 8 hours after inactivation of KIC12 (+rapalog) by NLS-mislocaliser or Lyn-
971 mislocaliser compared with corresponding control (without rapalog). Cells were
972 categorized as 'bloated FV' and 'non-bloated FV'. Results are displayed as percentage
973 of cells with bloated FV. n=3 (NLS) or n=4 (LYN) independent experiments were
974 performed with each n=19-80 (mean 41.3) parasites analysed per condition. P-values
975 determined by Welch's t-test. Representative DIC and fluorescence microscopy
976 images are shown in the right panel. Parasite cytoplasm was visualized with DHE.
977 Experimental setup shown in Figure S5D. Scale bar, 5 µm. **(G/I)** Area of the FV, area
978 of the parasite and area of FV divided by area of the corresponding parasite of the FV
979 of KIC12-2xFKBP-GFP-2xFKBP^{endo}+1xNLSmislocaliser (G) and KIC12-2xFKBP-
980 GFP-2xFKBP^{endo}+LYNmislocaliser (I) parasites analysed in 4F. Mean of each
981 independent experiment indicated by coloured triangle, individual datapoints by grey
982 dots. Data presented according to SuperPlot guidelines [123]; Error bars represent
983 mean ± SD. P-value determined by paired t-test. **(H/J)** Area of FV of individual cells
984 plotted versus the area of the corresponding parasite in KIC12-2xFKBP-GFP-
985 2xFKBP^{endo}+1xNLSmislocaliser and KIC12-2xFKBP-GFP-2xFKBP^{endo}+Lyn-
986 mislocaliser parasites of the experiments shown in (F,G and I). Line represents linear
987 regression with error indicated by dashed line. Ten representative DIC images of each
988 independent experiment are shown in Figure S5E,F **(K)** Number of vesicles per

989 parasite in trophozoites determined by live-cell fluorescence microscopy (DIC) in
990 KIC12-2xFKBP-GFP-2xFKBP^{endo}+1xNLSmislocaliser and KIC12-2xFKBP-GFP-
991 2xFKBP^{endo}+Lyn-mislocaliser parasites with and without rapalog addition. Three
992 independent experiments with n=10-56 (mean 28) parasites analysed per condition
993 and experiment Data presented according to SuperPlot guidelines [123]; Mean of each
994 independent experiment indicated by coloured triangle, individual datapoints by grey
995 dots. Error bars represent mean ± SD. P-value determined by paired t-test.
996 Representative DIC images are displayed. **(L)** Parasite survival rate (% survival
997 compared to control without DHA) 66 h after 6 h DHA treatment in standard RSA.
998 Three independent experiments, P-value determined by paired t-test. Green dashed
999 line indicates 1% ART resistance cut-off [23]. 3151-4273 (mean 3690) cells for control
1000 and 6209-18941 (mean 12290) cells for DHA treated samples were counted. Nuclei
1001 were stained with DAPI (A, B). Experimental setup shown in Figure S5G.Scale bars,
1002 5 µm.
1003
1004 **Figure 5: Type of domain found in K13 compartment proteins coincide with**
1005 **functional group**
1006 **(A)** K13-compartment members shown to scale with domains indicated that were
1007 identified from AlphaFold structure predictions. Newly identified domains (i.e. domains
1008 not previously identified by sequence homology) are shown in colours, previously
1009 known domains are shown in grey. A brief summary of the function of each newly
1010 identified domain and Interpro IDs of all domains can be found in supplementary figure
1011 S8. **(B)** Alphafold prediction of each newly identified domain is shown in the same
1012 colour as in A and aligned with the most similar domain from the PDB. PDB ID and
1013 alignment details are indicated beneath each set of aligned domains. Root mean
1014 square deviations (RMSD) for all comparisons are given. **(C)** Domain organizations of
1015 human GGA1 (hGGA1), KIC4 and human AP-2 subunit beta 1 (hAP2B1) are shown
1016 (not to scale). Domains are coloured as in A and B. **(D)** Domain organizations of KIC5
1017 and human AP-2 subunit alpha 1 (hAP2A1) are shown (not to scale). Domains are
1018 coloured as in A, B and C. (**E**) Table summarising K13 compartment proteins
1019 according to property (presence of vesicle trafficking domain (VTD)) and function.
1020
1021 **Figure S1: Validation of generated transgenic cell lines**
1022 Confirmatory PCR of unmodified wildtype (WT) and transgenic knock-in (KI) / targeted-
1023 gene-disruption (TGD) cell lines to confirm correct genomic integration at the 3'- and
1024 5'-end of the locus. Oligonucleotides used are listed in Table S2. **(A)** MCA2^{Y1344STOP}-
1025 GFP^{endo}; **(B)** MCA2-3xHA^{endo}; **(C)** MyoF-2xFKBP-GFP-2xFKBP^{endo}; **(D)** MyoF-
1026 2xFKBP-GFP^{endo}; **(E)** MyoF-3xHA^{endo}; **(F)** KIC11-2xFKBP-GFP-2xFKBP^{endo}; **(G)**
1027 KIC12-2xFKBP-GFP-2xFKBP^{endo}; **(H)** PF3D7_0907200-2xFKBP-GFP-2xFKBP^{endo}; **(I)**

1028 VPS51-2xFKBP-GFP-2xFKBP^{endo}; **(J)** PF3D7_1365800-2xFKBP-GFP-2xFKBP^{endo};
1029 **(K)** UIS14-2xFKBP-GFP-2xFKBP^{endo}; **(L)** PF3D7_1447800-2xFKBP-GFP-
1030 2xFKBP^{endo}; **(M)** VPS51-TGD^{endo}; **(N)** UIS14-TGD^{endo}. Right panel in **(A and B)**
1031 Western Blot analysis of **(A)** MCA2^{Y1344STOP}-GFP^{endo} cell line using mouse anti-GFP
1032 to detect the tagged fusion protein (upper panel) and rabbit anti-aldolase to control for
1033 equal loading (lower panel)(expected molecular weight for MCA2^{Y1344STOP}-GFP fusion
1034 proteins: 187 kDa) and **(B)** wildtype (3D7) and knock-in MCA2-3xHA^{endo} cell line using
1035 mouse anti-HA to detect the tagged full-length protein (upper panel) and rabbit anti-
1036 aldolase to control for equal loading (lower panel) (expected molecular weight for
1037 MCA2-3xHA fusion protein: 281 kDa). Protein size is indicated in kDa.
1038
1039 **Figure S2: Additional data for MCA2**
1040 **(A)** Localisation of truncated the MCA2TGD-GFP by live-cell microscopy across the
1041 intra-erythrocytic development cycle. Nuclei were stained with DAPI. Scale bar, 5 µm.
1042 **(B)** IFA microscopy images of acetone-fixed parasites expressing MCA2-3xHA with
1043 episomally expressed mCherry-K13 across the intra-erythrocytic development cycle.
1044 Nuclei were stained with DAPI. Scale bar, 5µm. Foci were categorized into 'overlap'
1045 (black), 'partial overlap' (dark grey) and 'no overlap' (light grey) in n=30 parasites.
1046 Schematic representation of the cell lines depicted above the corresponding panel.
1047
1048 **Figure S3: Additional data for MyoF**
1049 **(A)** Localisation of MyoF-2xFKBP-GFP by live-cell microscopy across the intra-
1050 erythrocytic development cycle. Nuclei were stained with DAPI. Scale bar, 5 µm. **(B)**
1051 IFA microscopy images of acetone-fixed parasites expressing MyoF-3xHA with
1052 episomally expressed mCherry-K13 across the intra-erythrocytic development cycle.
1053 Nuclei were stained with DAPI. Scale bar, 5µm. Foci were categorized into 'overlap'
1054 (black), 'partial overlap' (dark grey), close foci (light blue) and 'non overlap' (light grey)
1055 in n=31 parasites. Scale bar, 5µm. **(C)** Live-cell microscopy of knock sideways (+
1056 rapalog) and control (without rapalog) MyoF-2xFKBP-GFP-
1057 2xFKBP^{endo}+1xNLSmislocaliser parasites at 0, 1, 2, 4 and 22 hours after the induction
1058 of knock-sideways by addition of rapalog. **(D)** Individual growth curves of MyoF-
1059 2xFKBP-GFP-2xFKBP^{endo}+1xNLSmislocaliser with (red) or without (blue) addition of
1060 rapalog shown in Figure 2F. **(E)** Experimental setup of the bloated food vacuole assay
1061 shown in Figure 2H. **(F)** Experimental setup of the RSA shown in Figure 2I. Schematic
1062 representation of the cell lines depicted above the corresponding panel.
1063
1064 **Figure S4: Additional data for KIC11**
1065 **(A)** Individual growth curves of knock sideways (+ rapalog) and control (without
1066 rapalog) of KIC11-2xFKBP-GFP-2xFKBP^{endo}+1xNLSmislocaliser shown in Figure 3D.

1067 **(B)** Parasite stage distribution in Giemsa smears at the time points (average hours
1068 post invasion, h) indicated above each bar in tightly synchronised (±4h) KIC11-
1069 2xFKBP-GFP-2xFKBP^{endo}+1xNLSmislocaliser parasites (rapalog addition at 4 hpi, 20
1070 hpi, or 32 hpi and control) parasite cultures over two consecutive cycles (last time point
1071 in cycle 3). A second replicate is shown in Figure 3E. **(C)** Experimental setup of the
1072 bloated food vacuole assay shown in Figure 3H. **(D)** Experimental setup of the RSA
1073 shown in Figure 3I. Schematic representation of the cell lines depicted above the
1074 corresponding panel.
1075
1076 **Figure S5: Additional data for KIC12**
1077 **(A)** Localisation of KIC12-2xFKBP-GFP-2xFKBP by live-cell microscopy across the
1078 intra-erythrocytic development cycle. Nuclei were stained with DAPI. Scale bar, 5 µm.
1079 Expanded panel of Figure 4A **(B)** Individual growth curves of knock sideways (+
1080 rapalog; red) and control (without rapalog; blue) KIC12-2xFKBP-GFP-
1081 2xFKBP^{endo}+1xNLSmislocaliser shown in Figure 4D. **(C)** Individual growth curves of
1082 knock sideways (+ rapalog; red) and control (without rapalog; blue) KIC12-2xFKBP-
1083 GFP-2xFKBP^{endo}+LYNmislocaliser shown in Figure 4D. **(D)** Experimental setup of the
1084 bloated food vacuole assay shown in Figure 4F-G. **(E)** Representative images of
1085 bloated food vacuole assay knock sideways (+ rapalog; bottom row) and control
1086 (without rapalog; top row) KIC12-2xFKBP-GFP-2xFKBP^{endo}+1xNLSmislocaliser Scale
1087 bar, 5 µm. **(F)** Representative images of knock sideways (+ rapalog, top row) and
1088 control (without rapalog; bottom row) KIC12-2xFKBP-GFP-
1089 2xFKBP^{endo}+LYNmislocaliser parasites from bloated food vacuole assay. Scale bar, 5
1090 µm. **(G)** Experimental setup of the RSA shown in Figure 4J. Schematic representation
1091 of the cell lines depicted above the corresponding panel.
1092
1093 **Figure S6: Candidate proteins not associated with the K13 compartment**
1094 **(A)** Live cell microscopy images of parasites endogenously expressing VPS51-
1095 2xFKBP-GFP-2xFKBP with episomally expressed mCherry-K13 across the intra-
1096 erythrocytic development cycle. Scale bar, 5 µm. **(B)** Localisation of truncated
1097 VPS51TGD-GFP fusion protein by live-cell microscopy across the intra-erythrocytic
1098 development cycle. Nuclei were stained with DAPI. Scale bar, 5 µm. Schematic
1099 representation of the truncation strategy depicted above the panel, numbers indicating
1100 AA. **(C)** Relative growth of VPS51TGD and UIS14TGD parasites compared to 3D7
1101 wild type parasites after two cycles. Four independent growth experiments. P-values
1102 determined by one-sample t-test. **(D)** Live cell microscopy images of parasites
1103 endogenously expressing UIS14-2xFKBP-GFP-2xFKBP with episomally expressed
1104 mCherry-K13 across the intra-erythrocytic development cycle. Scale bar, 5 µm. **(E)**
1105 Localisation of truncated UIS14TGD-GFP fusion protein by live-cell microscopy across

1106 the intra-erythrocytic development cycle. Nuclei were stained with DAPI. Scale bar, 5
1107 µm. Schematic representation of the truncation strategy depicted above the panel,
1108 numbers indicating AA. **(F)** Live cell microscopy images of parasites endogenously
1109 expressing PF3D7_1447800-2xFKBP-GFP-2xFKBP with episomally expressed
1110 mCherry-K13 across the intra-erythrocytic development cycle. Nuclei were stained
1111 with DAPI. Scale bar, 5 µm. **(G)** Live cell microscopy images of parasites
1112 endogenously expressing PF3D7_0907200-2xFKBP-GFP-2xFKBP with episomally
1113 expressed mCherry-K13 across the intra-erythrocytic development cycle. Scale bar, 5
1114 µm. Schematic representation of relevant features of each cell line depicted above
1115 the corresponding panel.
1116
1117 **Figure S7: 3D7_1365800 an AH domain containing protein is dispensable for**
1118 **asexual parasite development**
1119 **(A)** Live cell microscopy images of parasites endogenously expressing
1120 PF3D7_1365800-2xFKBP-GFP-2xFKBP by live-cell microscopy across the intra-
1121 erythrocytic development cycle. Nuclei were stained with DAPI. Scale bar, 5 µm. (**B)**
1122 Expression of PF3D7_1365800-2xFKBP-GFP-2xFKBP with episomally expressed
1123 mCherry-K13. Scale bar, 5 µm. **(C)** Live-cell microscopy of knock sideways (+ rapalog)
1124 and control (without rapalog) PF3D7_1365800-2xFKBP-GFP-
1125 2xFKBP^{endo}+1xNLSmislocaliser parasites 16 hours after the induction of knock-
1126 sideways by addition of rapalog. Scale bar, 5 µm. **(D)** Individual growth curves of
1127 PF3D7_1365800-2xFKBP-GFP-2xFKBP^{endo}+1xNLSmislocaliser with (red) or without
1128 (blue) addition of rapalog. Relative growth of knock sideways (+ rapalog) and control
1129 (without rapalog) PF3D7_1365800-2xFKBP-GFP-2xFKBP^{endo}+1xNLSmislocaliser
1130 parasites over two cycles. Three independent growth experiments were performed
1131 and mean relative parasitemia ± SD is shown. **(E)** Live cell microscopy images of
1132 parasites expressing PF3D7_1365800-2xFKBP-GFP-2xFKBP with episomally
1133 expressed Golgi marker GRASP-mCherry. Schematic representation of the cell lines
1134 depicted above the corresponding panel. Scale bar, 5 µm.
1135
1136 **Figure S8: Type of domain found in K13 compartment proteins coincide with**
1137 **functional group**
1138 **(A)** Full domain names and Interpro domain numbers for each domain in Figure 5 with
1139 indication in which K13-compartment members these proteins occur. For each newly
1140 identified domain a brief summary of its reported function is given. Colours are as in
1141 Figure 5. **(B)** Full length AlphaFold predictions for each K13-compartment member in
1142 which new domains were identified. New domains are coloured as in A and Figure 5.
1143 For UBP1 no prediction was available in the EMBL-AlphaFold database, and the
1144 structure was predicted in fragments as described in the methods. The predicted

fragment containing the newly identified domain is shown. **(C)** Full length structure of PF3D7_1365800, with AH domain in green. PF3D7_1365800 AH domain in green aligned with the most similar domain from the PDB. PDB ID and alignment details are indicated beneath each set of aligned domains. Brief summary about the AH domain and its Interpro ID are given.

Table S1: Selection characteristics of putative K13 compartment proteins selected for further characterization in this manuscript

Table S2: Oligonucleotides used for cloning and diagnostic genotyping PCR

References

1. WHO. World Malaria Report 2020. 2020.
2. Weiss DJ, Lucas TCD, Nguyen M, Nandi AK, Bisanzio D, Battle KE, et al. Mapping the global prevalence, incidence, and mortality of Plasmodium falciparum, 2000–17: a spatial and temporal modelling study. Lancet. 2019;394: 322–331. doi:10.1016/S0140-6736(19)31097-9
3. WHO. WHO Guidelines for malaria. WHO Guidelines for malaria. 2021.
4. Dondorp AM, Nosten F, Yi P, Das D, Phyo AP, Tarning J, et al. Artemisinin Resistance in Plasmodium falciparum Malaria. N Engl J Med. 2009;361: 455–467. doi:10.1056/NEJMoa0808859
5. Ashley EA, Dhorda M, Fairhurst RM, Amaratunga C, Lim P, Suon S, et al. Spread of Artemisinin Resistance in *Plasmodium falciparum* Malaria. N Engl J Med. 2014;371: 411–423. doi:10.1056/NEJMoa1314981
6. Amaratunga C, Sreng S, Suon S, Phelps ES, Stepniewska K, Lim P, et al. Artemisinin-resistant Plasmodium falciparum in Pursat province, western Cambodia: A parasite clearance rate study. Lancet Infect Dis. 2012;12: 851–858. doi:10.1016/S1473-3099(12)70181-0
7. Duru V, Khim N, Leang R, Kim S, Domergue A, Kloeung N, et al. Plasmodium falciparum dihydroartemisinin-piperaquine failures in Cambodia are associated with mutant K13 parasites presenting high survival rates in novel piperaquine in vitro assays: Retrospective and prospective investigations. BMC Med. 2015;13. doi:10.1186/s12916-015-0539-5
8. Woodrow CJ, White NJ. The clinical impact of artemisinin resistance in Southeast Asia and the potential for future spread. FEMS Microbiology Reviews. Oxford University Press; 2017. pp. 34–48. doi:10.1093/femsre/fuw037
9. Uwimana A, Umulisa N, Venkatesan M, Svigel SS, Zhou Z, Munyaneza T, et al. Association of Plasmodium falciparum kelch13 R561H genotypes with delayed parasite clearance in Rwanda: an open-label, single-arm, multicentre, therapeutic efficacy study. Lancet Infect Dis. 2021;21: 1120–1128. doi:10.1016/S1473-3099(21)00142-0
10. Uwimana A, Legrand E, Stokes BH, Ndikumana JLM, Warsame M, Umulisa N, et al. Emergence and clonal expansion of in vitro artemisinin-resistant Plasmodium falciparum kelch13 R561H mutant parasites in Rwanda. Nat Med.

2020;26. doi:10.1038/s41591-020-1005-2

11. Spring MD, Lin JT, Manning JE, Vanachayangkul P, Somethy S, Bun R, et al. Dihydroartemisinin-piperaquine failure associated with a triple mutant including kelch13 C580Y in Cambodia: An observational cohort study. Lancet Infect Dis. 2015;15: 683–691. doi:10.1016/S1473-3099(15)70049-6

12. Miotto O, Sekihara M, Tachibana SI, Yamauchi M, Pearson RD, Amato R, et al. Emergence of artemisinin-resistant Plasmodium falciparum with kelch13 C580Y mutations on the island of New Guinea. PLoS Pathog. 2020;16: e1009133. doi:10.1371/journal.ppat.1009133

13. Noedl H, Se Y, Schaecher K, Smith BL, Socheat D, Fukuda MM. Evidence of Artemisinin-Resistant Malaria in Western Cambodia. N Engl J Med. 2008;359: 2619–2620. doi:10.1056/NEJMc0805011

14. Mathieu LC, Cox H, Early AM, Mok S, Lazrek Y, Paquet JC, et al. Local emergence in amazonia of plasmodium falciparum K13 C580Y mutants associated with in vitro artemisinin resistance. Elife. 2020;9: 1–21. doi:10.7554/eLife.51015

15. Wasakul V, Disratthakit A, Mayxay M, Chindavongsa K, Sengsavath V, Thuy-Nhien N, et al. Malaria outbreak in Laos driven by a selective sweep for Plasmodium falciparum kelch13 R539T mutants: a genetic epidemiology analysis. Lancet Infect Dis. 2022;0. doi:10.1016/S1473-3099(22)00697-1

16. Phyo AP, Nkhoma S, Stepniewska K, Ashley EA, Nair S, McGready R, et al. Emergence of artemisinin-resistant malaria on the western border of Thailand: a longitudinal study. Lancet. 2012;379: 1960–1966. doi:10.1016/S0140-6736(12)60484-X

17. Klonis N, Xie SC, McCaw JM, Crespo-Ortiz MP, Zaloumis SG, Simpson JA, et al. Altered temporal response of malaria parasites determines differential sensitivity to artemisinin. Proc Natl Acad Sci U S A. 2013;110: 5157–5162. doi:10.1073/pnas.1217452110

18. Saralamba S, Pan-Ngum W, Maude RJ, Lee SJ, Tarning J, Lindegårdh N, et al. Intrahost modeling of artemisinin resistance in Plasmodium falciparum. Proc Natl Acad Sci U S A. 2011;108: 397–402. doi:10.1073/pnas.1006113108

19. Saunders DL, Vanachayangkul P, Lon C. Dihydroartemisinin–Piperaquine Failure in Cambodia. N Engl J Med. 2014;371: 484–485. doi:10.1056/nejmc1403007

20. Amaratunga C, Lim P, Suon S, Sreng S, Mao S, Sopha C, et al. Dihydroartemisinin-piperaquine resistance in Plasmodium falciparum malaria in Cambodia: A multisite prospective cohort study. Lancet Infect Dis. 2016;16: 357–365. doi:10.1016/S1473-3099(15)00487-9

21. Thanh NV, Thuy-Nhien N, Tuyen NTK, Tong NT, Nha-Ca NT, Dong LT, et al. Rapid decline in the susceptibility of Plasmodium falciparum to dihydroartemisinin-piperaquine in the south of Vietnam. Malar J. 2017;16: 1–10. doi:10.1186/s12936-017-1680-8

22. Watts RE, Odedra A, Marquart L, Webb L, Abd-Rahman AN, Cascales L, et al. Safety and parasite clearance of artemisinin-resistant Plasmodium falciparum infection: A pilot and a randomised volunteer infection study in Australia. PLoS Med. 2020;17. doi:10.1371/JOURNAL.PMED.1003203

23. Witkowski B, Amaratunga C, Khim N, Sreng S, Chim P, Kim S, et al. Novel

1237 phenotypic assays for the detection of artemisinin-resistant Plasmodium
1238 falciparum malaria in Cambodia: In-vitro and ex-vivo drug-response studies.
1239 Lancet Infect Dis. 2013;13: 1043–1049. doi:10.1016/S1473-3099(13)70252-4

1240 24. Ariey F, Witkowski B, Amaratunga C, Beghain J, Langlois AC, Khim N, et al. A
1241 molecular marker of artemisinin-resistant Plasmodium falciparum malaria.
1242 Nature. 2014;505: 50–55. doi:10.1038/nature12876

1243 25. Straimer J, Gnädig NF, Witkowski B, Amaratunga C, Duru V, Ramadani AP, et
1244 al. K13-propeller mutations confer artemisinin resistance in Plasmodium
1245 falciparum clinical isolates. Science (80-). 2015;347: 428–431.
1246 doi:10.1126/science.1260867

1247 26. Birnbaum J, Scharf S, Schmidt S, Jonscher E, Hoeijmakers WAM, Flemming
1248 S, et al. A Kelch13-defined endocytosis pathway mediates artemisinin
1249 resistance in malaria parasites. Science (80-). 2020;367: 51–59.
1250 doi:10.1126/science.aax4735

1251 27. Yang T, Yeoh LM, Tutor M V., Dixon MW, McMillan PJ, Xie SC, et al.
1252 Decreased K13 Abundance Reduces Hemoglobin Catabolism and Proteotoxic
1253 Stress, Underpinning Artemisinin Resistance. Cell Rep. 2019;29: 2917-
1254 2928.e5. doi:10.1016/j.celrep.2019.10.095

1255 28. Schumann R, Bischoff E, Klaus S, Möhring S, Flock J, Keller S, et al. Protein
1256 abundance and folding rather than the redox state of Kelch13 determine the
1257 artemisinin susceptibility of Plasmodium falciparum. Redox Biol. 2021;48.
1258 doi:10.1016/j.redox.2021.102177

1259 29. Siddiqui G, Srivastava A, Russell AS, Creek DJ. Multi-omics based
1260 identification of specific biochemical changes associated with PfKelch13-
1261 mutant artemisinin-resistant plasmodium falciparum. J Infect Dis. 2017;215:
1262 1435–1444. doi:10.1093/infdis/jix156

1263 30. Mok S, Stokes BH, Gnädig NF, Ross LS, Yeo T, Amaratunga C, et al.
1264 Artemisinin-resistant K13 mutations rewire Plasmodium falciparum's intra-
1265 erythrocytic metabolic program to enhance survival. Nat Commun. 2021;12.
1266 doi:10.1038/s41467-020-20805-w

1267 31. Behrens HM, Schmidt S, Spielmann T. The newly discovered role of
1268 endocytosis in artemisinin resistance. Med Res Rev. 2021; med.21848.
1269 doi:10.1002/med.21848

1270 32. Francis SE, Sullivan DJ, Goldberg DE. Hemoglobin metabolism in the malaria
1271 parasite Plasmodium falciparium. Annual Review of Microbiology. Annual
1272 Reviews 4139 El Camino Way, P.O. Box 10139, Palo Alto, CA 94303-0139,
1273 USA; 1997. pp. 97–123. doi:10.1146/annurev.micro.51.1.97

1274 33. Spielmann T, Gras S, Sabitzki R, Meissner M. Endocytosis in Plasmodium and
1275 Toxoplasma Parasites. Trends in Parasitology. Elsevier Ltd; 2020. pp. 520–
1276 532. doi:10.1016/j.pt.2020.03.010

1277 34. Krugliak M, Zhang J, Ginsburg H. Intraerythrocytic Plasmodium falciparum
1278 utilizes only a fraction of the amino acids derived from the digestion of host cell
1279 cytosol for the biosynthesis of its proteins. Mol Biochem Parasitol. 2002;119:
1280 249–256. doi:10.1016/S0166-6851(01)00427-3

1281 35. Sherman IW. Amino acid metabolism and protein synthesis in malarial
1282 parasites. Bulletin of the World Health Organization. World Health
1283 Organization; 1977. pp. 265–276.

36. Matz JM. Plasmodium's bottomless pit: properties and functions of the malaria parasite's digestive vacuole. Trends in Parasitology. Elsevier Ltd; 2022. pp. 525–543. doi:10.1016/j.pt.2022.02.010

37. Mesén-Ramírez P, Bergmann B, Elhabiri M, Zhu L, Thien H von, Castro-Peña C, et al. The parasitophorous vacuole nutrient pore is critical for drug access in malaria parasites and modulates the fitness cost of artemisinin resistance. Cell Host Microbe. 2021;0: 283. doi:10.1016/j.chom.2021.11.002

38. Bunditvorapoom D, Kochakarn T, Kotanan N, Modchang C, Kümpornsin K, Loesbanluechai D, et al. Fitness Loss under Amino Acid Starvation in Artemisinin-Resistant Plasmodium falciparum Isolates from Cambodia. Sci Rep. 2018;8: 1–9. doi:10.1038/s41598-018-30593-5

39. Milani KJ, Schneider TG, Taraschi TF. Defining the morphology and mechanism of the hemoglobin transport pathway in Plasmodium falciparum-infected erythrocytes. Eukaryot Cell. 2015;14: 415–426. doi:10.1128/EC.00267-14

40. Bakar NA, Klonis N, Hanssen E, Chan C, Tilley L. Digestive-vacuole genesis and endocytic processes in the early intraerythrocytic stages of Plasmodium falciparum. J Cell Sci. 2010;123: 441–450. doi:10.1242/jcs.061499

41. Smythe WA, Joiner KA, Hoppe HC. Actin is required for endocytic trafficking in the malaria parasite Plasmodium falciparum. Cell Microbiol. 2008;10: 452–464. doi:10.1111/j.1462-5822.2007.01058.x

42. Zhou HC, Gao YH, Zhong X, Wang H. Dynamin like protein 1 participated in the hemoglobin uptake pathway of Plasmodium falciparum. Chin Med J (Engl). 2009;122: 1686–1691. doi:10.3760/cma.j.issn.0366-6999.2009.14.015

43. Taraschi TF, O'Donnell M, Martinez S, Schneider T, Trelka D, Fowler VM, et al. Generation of an erythrocyte vesicle transport system by Plasmodium falciparum malaria parasites. Blood. 2003;102: 3420–3426. doi:10.1182/blood-2003-05-1448

44. Jonscher E, Flemming S, Schmitt M, Sabitzki R, Reichard N, Birnbaum J, et al. PfVPS45 Is Required for Host Cell Cytosol Uptake by Malaria Blood Stage Parasites. Cell Host Microbe. 2019;25: 166-173.e5. doi:10.1016/j.chom.2018.11.010

45. Mukherjee A, Crochetière M-È, Sergerie A, Amiar S, Thompson LA, Ebrahimzadeh Z, et al. A Phosphoinositide-Binding Protein Acts in the Trafficking Pathway of Hemoglobin in the Malaria Parasite Plasmodium falciparum. Soldati-Favre D, editor. MBio. 2022;13. doi:10.1128/mbio.03239-21

46. Wagner MP, Formaglio P, Gorgette O, Dziekan JM, Huon C, Berneburg I, et al. Human peroxiredoxin 6 is essential for malaria parasites and provides a host-based drug target. Cell Rep. 2022;39: 110923. doi:10.1016/j.celrep.2022.110923

47. Roux KJ, Kim DI, Raida M, Burke B. A promiscuous biotin ligase fusion protein identifies proximal and interacting proteins in mammalian cells. J Cell Biol. 2012;196: 801–810. doi:10.1083/jcb.201112098

48. Kimmel J, Kehrer J, Frischknecht F, Spielmann T. Proximity-dependent biotinylation approaches to study apicomplexan biology. Mol Microbiol. 2021. doi:10.1111/mmi.14815

49. Kono M, Herrmann S, Loughran NB, Cabrera A, Engelberg K, Lehmann C, et

1331 al. Evolution and architecture of the inner membrane complex in asexual and
1332 sexual stages of the malaria parasite. Mol Biol Evol. 2012;29: 2113–2132.
1333 doi:10.1093/molbev/mss081

1334 50. Parkyn Schneider M, Liu B, Glock P, Suttie A, McHugh E, Andrew D, et al.
1335 Disrupting assembly of the inner membrane complex blocks Plasmodium
1336 falciparum sexual stage development. Gilberger TW, editor. PLOS Pathog.
1337 2017;13: e1006659. doi:10.1371/journal.ppat.1006659

1338 51. Saini E, Zeeshan M, Brady D, Pandey R, Kaiser G, Koreny L, et al.
1339 Photosensitized INA-Labelled protein 1 (PhIL1) is novel component of the
1340 inner membrane complex and is required for Plasmodium parasite
1341 development. Sci Rep. 2017;7: 15577. doi:10.1038/s41598-017-15781-z

1342 52. Saini E, Sheokand PK, Sharma V, Agrawal P, Kaur I, Singh S, et al.
1343 Plasmodium falciparum PhIL1-associated complex plays an essential role in
1344 merozoite reorientation and invasion of host erythrocytes. PLOS Pathog.
1345 2021;17: e1009750. doi:10.1371/JOURNAL.PPAT.1009750

1346 53. Torres JA, Pasquarelli RR, Back PS, Moon AS, Bradley PJ. Identification and
1347 Molecular Dissection of IMC32, a Conserved Toxoplasma Inner Membrane
1348 Complex Protein That Is Essential for Parasite Replication. Boyle JP, editor.
1349 MBio. 2021;12. doi:10.1128/mBio.03622-20

1350 54. Wichers JS, Wunderlich J, Heincke D, Pazicky S, Strauss J, Schmitt M, et al.
1351 Identification of novel inner membrane complex and apical annuli proteins of
1352 the malaria parasite Plasmodium falciparum. Cell Microbiol. 2021;23: e13341.
1353 doi:10.1111/cmi.13341

1354 55. Rudlaff RM, Kraemer S, Streva VA, Dvorin JD. An essential contractile ring
1355 protein controls cell division in Plasmodium falciparum. Nat Commun. 2019;10:
1356 2181. doi:10.1038/s41467-019-10214-z

1357 56. Geiger M, Brown C, Wichers JS, Strauss J, Lill A, Thuenauer R, et al.
1358 Structural Insights Into PfARO and Characterization of its Interaction With
1359 PfAIP. J Mol Biol. 2020;432: 878–896. doi:10.1016/j.jmb.2019.12.024

1360 57. Koreny L, Zeeshan M, Barylyuk K, Tromer EC, van Hooff JJE, Brady D, et al.
1361 Molecular characterization of the conoid complex in Toxoplasma reveals its
1362 conservation in all apicomplexans, including Plasmodium species. Duffy M,
1363 editor. PLOS Biol. 2021;19: e3001081. doi:10.1371/journal.pbio.3001081

1364 58. Thommen BT, Dziekan JM, Achcar F, Tjia S, Passecker A, Buczak K, et al.
1365 FKBP35 secures ribosome homeostasis in Plasmodium falciparum. bioRxiv.
1366 2022; 2022.12.09.519720. doi:10.1101/2022.12.09.519720

1367 59. Kumar R, Adams B, Musiyenko A, Shulyayeva O, Barik S. The FK506-binding
1368 protein of the malaria parasite, Plasmodium falciparum, is a FK506-sensitive
1369 chaperone with FK506-independent calcineurin-inhibitory activity. Mol Biochem
1370 Parasitol. 2005;141: 163–73. doi:10.1016/j.molbiopara.2005.02.007

1371 60. Boucher MJ, Ghosh S, Zhang L, Lal A, Jang SW, Ju A, et al. Integrative
1372 proteomics and bioinformatic prediction enable a high-confidence apicoplast
1373 proteome in malaria parasites. Striepen B, editor. PLoS Biol. 2018;16:
1374 e2005895. doi:10.1371/journal.pbio.2005895

1375 61. MalariaGEN, Ahouidi A, Ali M, Almagro-Garcia J, Amambua-Ngwa A,
1376 Amaratunga C, et al. An open dataset of Plasmodium falciparum genome
1377 variation in 7,000 worldwide samples. Wellcome open Res. 2021;6: 42.

1378 doi:10.12688/wellcomeopenres.16168.2
1379 62. Wichers JS, Tonkin-Hill G, Thye T, Krumkamp R, Kreuels B, Strauss J, et al.
1380 Common virulence gene expression in adult first-time infected malaria patients
1381 and severe cases. Elife. 2021;10. doi:10.7554/eLife.69040
1382 63. Birnbaum J, Flemming S, Reichard N, Soares AB, Mesén-Ramírez P,
1383 Jonscher E, et al. A genetic system to study Plasmodium falciparum protein
1384 function. Nat Methods. 2017;14: 450–456. doi:10.1038/nmeth.4223
1385 64. Lazarus MD, Schneider TG, Taraschi TF. A new model for hemoglobin
1386 ingestion and transport by the human malaria parasite Plasmodium falciparum.
1387 J Cell Sci. 2008;121: 1937–1949. doi:10.1242/jcs.023150
1388 65. Wichers JS, Scholz JAM, Strauss J, Witt S, Lill A, Ehnold L-I, et al. Dissecting
1389 the Gene Expression, Localisation, Membrane Topology, and Function of the
1390 Plasmodium falciparum STEVOR Protein Family. Boothroyd JC, editor. MBio.
1391 2019;10: e01500-19. doi:10.1128/mBio.01500-19
1392 66. Subudhi AK, O'Donnell AJ, Ramaprasad A, Abkallo HM, Kaushik A, Ansari
1393 HR, et al. Malaria parasites regulate intra-erythrocytic development duration
1394 via serpentine receptor 10 to coordinate with host rhythms. Nat Commun.
1395 2020;11. doi:10.1038/s41467-020-16593-y
1396 67. Robinson MS, Sahlender DA, Foster SD. Rapid Inactivation of Proteins by
1397 Rapamycin-Induced Rerouting to Mitochondria. Dev Cell. 2010;18: 324–331.
1398 doi:10.1016/j.devcel.2009.12.015
1399 68. Haruki H, Nishikawa J, Laemmli UK. The Anchor-Away Technique: Rapid,
1400 Conditional Establishment of Yeast Mutant Phenotypes. Mol Cell. 2008;31:
1401 925–932. doi:10.1016/j.molcel.2008.07.020
1402 69. Sijwali PS, Rosenthal PJ. Gene disruption confirms a critical role for the
1403 cysteine protease falcipain-2 in hemoglobin hydrolysis by Plasmodium
1404 falciparum. Proc Natl Acad Sci U S A. 2004;101: 4384–4389.
1405 doi:10.1073/pnas.0307720101
1406 70. Otto TD, Wilinski D, Assefa S, Keane TM, Sarry LR, Böhme U, et al. New
1407 insights into the blood-stage transcriptome of Plasmodium falciparum using
1408 RNA-Seq. Mol Microbiol. 2010;76: 12–24. doi:10.1111/j.1365-
1409 2958.2009.07026.x
1410 71. Kimmel J, Schmitt M, Sinner A, Jansen P, Mainye S, Ramón-Zamorano G, et
1411 al. Gene-by-gene screen of the unknown proteins encoded on P. falciparum
1412 chromosome 3. bioRxiv. 2022; 2022.07.07.499005.
1413 doi:10.1101/2022.07.07.499005
1414 72. Jumper J, Evans R, Pritzel A, Green T, Figurnov M, Ronneberger O, et al.
1415 Highly accurate protein structure prediction with AlphaFold. Nature. 2021;596:
1416 583–589. doi:10.1038/s41586-021-03819-2
1417 73. Cherfils J. Structural mimicry of DH domains by Arfaptin suggests a model for
1418 the recognition of Rac-GDP by its guanine nucleotide exchange factors. FEBS
1419 Lett. 2001;507: 280–284. doi:10.1016/S0014-5793(01)02970-2
1420 74. Tarricone C, Xiao B, Justin N, Walker PA, Rittinger K, Gamblin SJ, et al. The
1421 structural basis of Arfaptin-mediated cross-talk between Rac and Arf signalling
1422 pathways. Nature. 2001;411: 215–219. doi:10.1038/35075620
1423 75. McGovern OL, Rivera-Cuevas Y, Kannan G, Narwold AJ, Carruthers VB.
1424 Intersection of endocytic and exocytic systems in Toxoplasma gondii. Traffic.

2018;19: 336–353. doi:10.1111/tra.12556

76. Struck NS, de Souza Dias S, Langer C, Marti M, Pearce JA, Cowman AF, et al. Re-defining the Golgi complex in Plasmodium falciparum using the novel Golgi marker PfGRASP. J Cell Sci. 2005;118: 5603–5613. doi:10.1242/jcs.02673

77. Varadi M, Anyango S, Deshpande M, Nair S, Natassia C, Yordanova G, et al. AlphaFold Protein Structure Database: Massively expanding the structural coverage of protein-sequence space with high-accuracy models. Nucleic Acids Res. 2022;50: D439–D444. doi:10.1093/nar/gkab1061

78. Hirst J, Lui WWY, Bright NA, Totty N, Seaman MNJ, Robinson MS. A family of proteins with γ-adaptin and VHS domains that facilitate trafficking between the trans-golgi network and the vacuole/lysosome. J Cell Biol. 2000;149: 67–79. doi:10.1083/jcb.149.1.67

79. Dell'Angelica EC, Puertollano R, Mullins C, Aguilar RC, Vargas JD, Hartnell LM, et al. GGAs: A family of ADP ribosylation factor-binding proteins related to adaptors and associated with the Golgi complex. J Cell Biol. 2000;149: 81–93. doi:10.1083/jcb.149.1.81

80. Blum M, Chang HY, Chuguransky S, Grego T, Kandasaamy S, Mitchell A, et al. The InterPro protein families and domains database: 20 years on. Nucleic Acids Res. 2021;49: D344–D354. doi:10.1093/nar/gkaa977

81. Koreny L, Mercado-Saavedra BN, Klinger CM, Barylyuk K, Butterworth S, Hirst J, et al. Stable and ancient endocytic structures navigate the complex pellicle of apicomplexan parasites. bioRxiv. 2022; 2022.06.02.494549. doi:10.1101/2022.06.02.494549

82. Tanna CE, Goss LB, Ludwig CG, Chen PW. Arf GAPs as regulators of the actin cytoskeleton—An update. International Journal of Molecular Sciences. MDPI AG; 2019. doi:10.3390/ijms20020442

83. Kjos I, Vestre K, Guadagno NA, Borg Distefano M, Progida C. Rab and Arf proteins at the crossroad between membrane transport and cytoskeleton dynamics. Biochimica et Biophysica Acta - Molecular Cell Research. Elsevier B.V.; 2018. pp. 1397–1409. doi:10.1016/j.bbamcr.2018.07.009

84. Hunt P, Afonso A, Creasey A, Culleton R, Sidhu ABS, Logan J, et al. Gene encoding a deubiquitinating enzyme is mutated in artesunate- and chloroquine-resistant rodent malaria parasites. Mol Microbiol. 2007;65: 27–40. doi:10.1111/j.1365-2958.2007.05753.x

85. Sun D, Leung CL, Liem RK. Characterization of the microtubule binding domain of microtubule actin crosslinking factor (MACF): identification of a novel group of microtubule associated proteins. J Cell Sci. 2001;114: 161–172. doi:10.1242/jcs.114.1.161

86. Sahu SC, Swanson KA, Kang RS, Huang K, Brubaker K, Ratcliff K, et al. Conserved Themes in Target Recognition by the PAH1 and PAH2 Domains of the Sin3 Transcriptional Corepressor. J Mol Biol. 2008;375: 1444–1456. doi:10.1016/j.jmb.2007.11.079

87. Brubaker K, Cowley SM, Huang K, Loo L, Yochum GS, Ayer DE, et al. Solution structure of the interacting domains of the mad-sin3 complex: Implications for recruitment of a chromatin-modifying complex. Cell. 2000;103: 655–665. doi:10.1016/S0092-8674(00)00168-9

1472 88. Doherty GJ, McMahon HT. Mechanisms of Endocytosis. Annu Rev Biochem.
1473 2009;78: 857–902. doi:10.1146/annurev.biochem.78.081307.110540
1474 89. Kaksonen M, Roux A. Mechanisms of clathrin-mediated endocytosis. Nature
1475 Reviews Molecular Cell Biology. Nature Publishing Group; 2018. pp. 313–326.
1476 doi:10.1038/nrm.2017.132
1477 90. Thottacherry JJ, Sathe M, Prabhakara C, Mayor S. Spoiled for choice: Diverse
1478 endocytic pathways function at the cell surface. Annual Review of Cell and
1479 Developmental Biology. Annual Reviews Inc.; 2019. pp. 55–84.
1480 doi:10.1146/annurev-cellbio-100617-062710
1481 91. Henrici RC, Edwards RL, Zoltner M, van Schalkwyk DA, Hart MN, Mohring F,
1482 et al. The plasmodium falciparum artemisinin susceptibility-associated ap-2
1483 adaptin μ subunit is clathrin independent and essential for schizont maturation.
1484 MBio. 2020;11. doi:10.1128/mBio.02918-19
1485 92. Schmid EM, Ford MGJ, Burtey A, Praefcke GJK, Peak-Chew S-Y, Mills IG, et
1486 al. Role of the AP2 β-Appendage Hub in Recruiting Partners for Clathrin-
1487 Coated Vesicle Assembly. Hughson F, editor. PLoS Biol. 2006;4: e262.
1488 doi:10.1371/journal.pbio.0040262
1489 93. Perrais D. Cellular and structural insight into dynamin function during endocytic
1490 vesicle formation: a tale of 50 years of investigation. Biosci Rep. 2022;42.
1491 doi:10.1042/bsr20211227
1492 94. Heredero-Bermejo I, Varberg JM, Charvat R, Jacobs K, Garbuz T, Sullivan
1493 WJ, et al. TgDrpC, an atypical dynamin-related protein in *Toxoplasma gondii,*
1494 is associated with vesicular transport factors and parasite division. Mol
1495 Microbiol. 2019;111: 46–64. doi:10.1111/mmi.14138
1496 95. Wall RJ, Zeeshan M, Katris NJ, Limenitakis R, Rea E, Stock J, et al.
1497 Systematic analysis of Plasmodium myosins reveals differential expression,
1498 localisation, and function in invasive and proliferative parasite stages. Cell
1499 Microbiol. 2019;21. doi:10.1111/cmi.13082
1500 96. DePina AS, Langford GM. Vesicle transport: The role of actin filaments and
1501 myosin motors. Microsc Res Tech. 1999;47: 93–106. doi:10.1002/(SICI)1097-
1502 0029(19991015)47:2<93::AID-JEMT2>3.0.CO;2-P
1503 97. Chakrabarti R, Lee M, Higgs HN. Multiple roles for actin in secretory and
1504 endocytic pathways. Current Biology. Cell Press; 2021. pp. R603–R618.
1505 doi:10.1016/j.cub.2021.03.038
1506 98. Zhang M, Wang C, Otto TD, Oberstaller J, Liao X, Adapa SR, et al.
1507 Uncovering the essential genes of the human malaria parasite Plasmodium
1508 falciparum by saturation mutagenesis. Science. 2018;360: eaap7847.
1509 doi:10.1126/science.aap7847
1510 99. Carmeille R, Schiano Lomoriello P, Devarakonda PM, Kellermeier JA, Heaslip
1511 AT. Actin and an unconventional myosin motor, TgMyoF, control the
1512 organization and dynamics of the endomembrane network in Toxoplasma
1513 gondii. Gubbels M-J, editor. PLOS Pathog. 2021;17: e1008787.
1514 doi:10.1371/journal.ppat.1008787
1515 100. Jacot D, Daher W, Soldati-Favre D. Toxoplasma gondii myosin F, an essential
1516 motor for centrosomes positioning and apicoplast inheritance. EMBO J.
1517 2013;32: 1702–1716. doi:10.1038/emboj.2013.113
1518 101. Kumari V, Prasad KM, Kalia I, Sindhu G, Dixit R, Rawat DS, et al. Dissecting

1519 the role of Plasmodium Metacaspase-2 in malaria gametogenesis and
1520 sporogony. Emerg Microbes Infect. 2022; 1–50.
1521 doi:10.1080/22221751.2022.2052357

1522 102. Fonager J, Franke-Fayard BMD, Adams JH, Ramesar J, Klop O, Khan SM, et
1523 al. Development of the piggyBac transposable system for Plasmodium berghei
1524 and its application for random mutagenesis in malaria parasites. BMC
1525 Genomics. 2011;12. doi:10.1186/1471-2164-12-155

1526 103. Kumari V, Singh AP, Singh J, Sharma R, Akhter M, Mishra PK, et al.
1527 Biochemical characterization of unusual cysteine protease of P. falciparum,
1528 metacaspase-2 (MCA-2). Mol Biochem Parasitol. 2018;220: 28–41.
1529 doi:10.1016/j.molbiopara.2018.01.001

1530 104. Vandana, Shankar S, Prasad KM, Kashif M, Kalia I, Rai R, et al. A nonpeptidyl
1531 molecule modulates apoptosis-like cell death by inhibiting P. Falciparum
1532 metacaspase-2. Biochem J. 2020;477: 1323–1344. doi:10.1042/BCJ20200050

1533 105. Vandana , Pandey R, Srinivasan E, Kalia I, Singh AP, Saxena A, et al.
1534 Plasmodium falciparum metacaspase-2 capture its natural substrate in a non-
1535 canonical way . J Biochem. 2021;170: 639–653. doi:10.1093/jb/mvab086

1536 106. Bushell E, Gomes AR, Sanderson T, Anar B, Girling G, Herd C, et al.
1537 Functional Profiling of a Plasmodium Genome Reveals an Abundance of
1538 Essential Genes. Cell. 2017;170: 260-272.e8. doi:10.1016/j.cell.2017.06.030

1539 107. Walliker D, Quakyi IA, Wellems TE, McCutchan TF, Szarfman A, London WT,
1540 et al. Genetic analysis of the human malaria parasite Plasmodium falciparum.
1541 Science (80-). 1987;236: 1661–6.

1542 108. Trager W, Jensen JB. Continuous culture of Plasmodium falciparum: its impact
1543 on malaria research. Int J Parasitol. 1997;27: 989–1006. doi:10.1016/S0020-
1544 7519(97)00080-5

1545 109. Rivadeneira E, Wasserman M, Espinal C. Separation and Concentration of
1546 Schizonts of Plasmodium falciparum by Percoll Gradients. J Protozool.
1547 1983;30: 367–370. doi:10.1111/j.1550-7408.1983.tb02932.x

1548 110. Lambros C, Vanderberg JP. Synchronization of Plasmodium falciparum
1549 Erythrocytic Stages in Culture. J Parasitol. 1979;65: 418. doi:10.2307/3280287

1550 111. Mesén-Ramírez P, Bergmann B, Tran TT, Garten M, Stäcker J, Naranjo-Prado
1551 I, et al. EXP1 is critical for nutrient uptake across the parasitophorous vacuole
1552 membrane of malaria parasites. de Koning-Ward TF, editor. PLoS Biol.
1553 2019;17: e3000473. doi:10.1371/journal.pbio.3000473

1554 112. Wichers-Misterek JS, Binder AM, Mesén-Ramírez P, Dorner LP, Safavi S,
1555 Fuchs G, et al. A microtubule associated protein is essential for malaria
1556 parasite transmission. bioRxiv. 2022; 2022.10.18.512810.
1557 doi:10.1101/2022.10.18.512810

1558 113. Moon RW, Hall J, Rangkuti F, Ho YS, Almond N, Mitchell GH, et al. Adaptation
1559 of the genetically tractable malaria pathogen Plasmodium knowlesi to
1560 continuous culture in human erythrocytes. Proc Natl Acad Sci. 2013;110: 531–
1561 536. doi:10.1073/pnas.1216457110

1562 114. Ganesan SM, Morrisey JM, Ke H, Painter HJ, Laroiya K, Phillips MA, et al.
1563 Yeast dihydroorotate dehydrogenase as a new selectable marker for
1564 Plasmodium falciparum transfection. Mol Biochem Parasitol. 2011;177: 29–34.
1565 doi:10.1016/j.molbiopara.2011.01.004

115. Grüring C, Spielmann T. Imaging of live malaria blood stage parasites. Methods Enzymol. 2012;506: 81–92. doi:10.1016/B978-0-12-391856-7.00029-9

116. Malleret B, Claser C, Ong ASM, Suwanarusk R, Sriprawat K, Howland SW, et al. A rapid and robust tri-color flow cytometry assay for monitoring malaria parasite development. Sci Rep. 2011;1: 118. doi:10.1038/srep00118

117. Mesén-Ramírez P, Reinsch F, Blancke Soares A, Bergmann B, Ullrich AK, Tenzer S, et al. Stable Translocation Intermediates Jam Global Protein Export in Plasmodium falciparum Parasites and Link the PTEX Component EXP2 with Translocation Activity. Soldati-Favre D, editor. PLoS Pathog. 2016;12: e1005618. doi:10.1371/journal.ppat.1005618

118. Mirdita M, Schütze K, Moriwaki Y, Heo L, Ovchinnikov S, Steinegger M. ColabFold: making protein folding accessible to all. Nat Methods. 2022;19: 679–682. doi:10.1038/s41592-022-01488-1

119. Gibrat JF, Madej T, Bryant SH. Surprising similarities in structure comparison. Curr Opin Struct Biol. 1996;6: 377–385. doi:10.1016/S0959-440X(96)80058-3

120. Aurrecoechea C, Brestelli J, Brunk BP, Dommer J, Fischer S, Gajria B, et al. PlasmoDB: a functional genomic database for malaria parasites. Nucleic Acids Res. 2009;37: D539–D543. doi:10.1093/nar/gkn814

121. Schindelin J, Arganda-Carreras I, Frise E, Kaynig V, Longair M, Pietzsch T, et al. Fiji: an open-source platform for biological-image analysis. Nat Methods. 2012;9: 676–682. doi:10.1038/nmeth.2019

122. Davis MW, Jorgensen EM. ApE, A Plasmid Editor: A Freely Available DNA Manipulation and Visualization Program. Front Bioinforma. 2022;2: 5. doi:10.3389/fbinf.2022.818619

123. Lord SJ, Velle KB, Mullins RD, Fritz-Laylin LK. SuperPlots: Communicating reproducibility and variability in cell biology. J Cell Biol. 2020;219. doi:10.1083/jcb.202001064

Figure 1

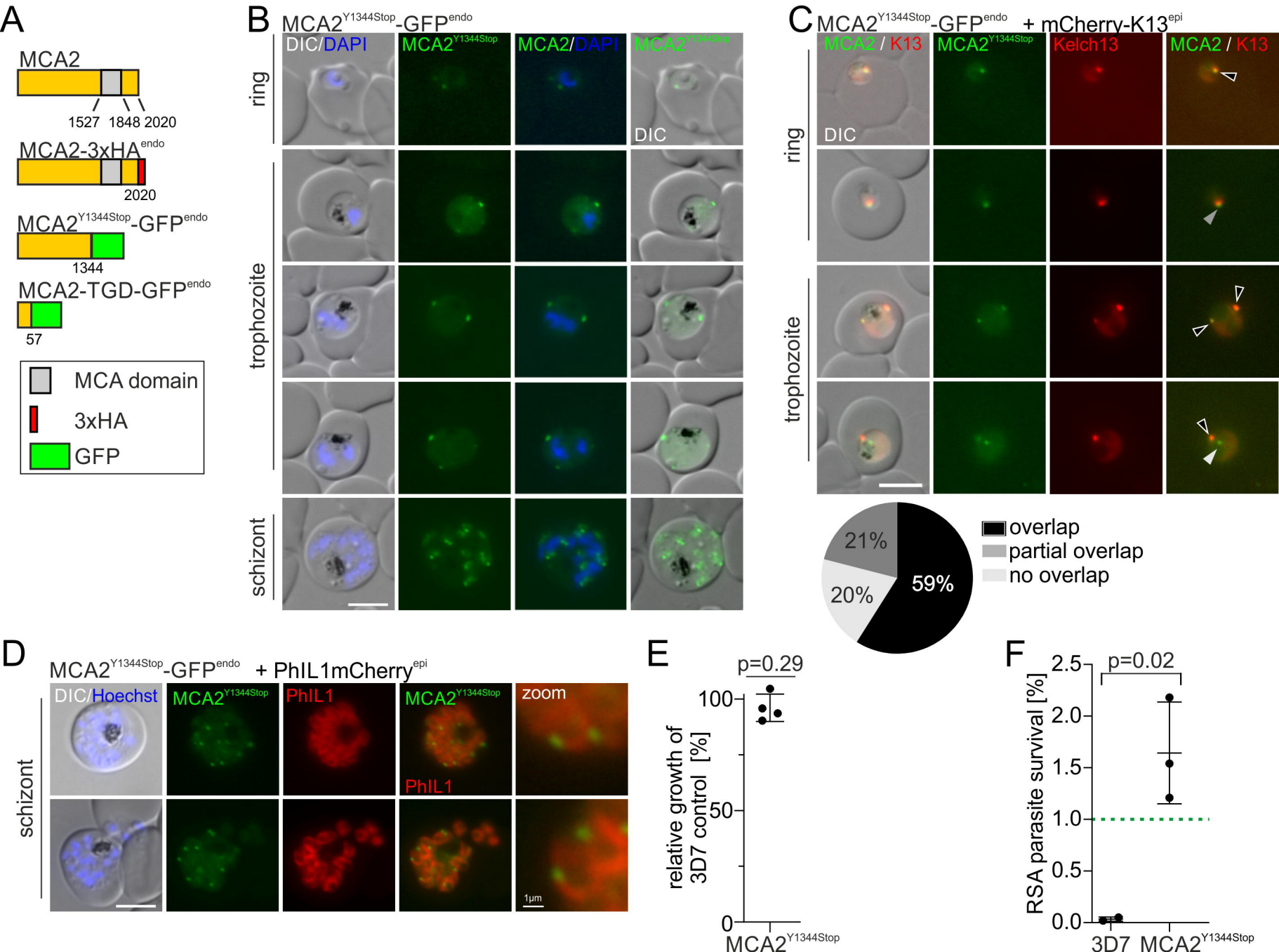
A
MCA2
1527 1848 2020
MCA2-3xHA endo
2020
MCA2 Y1344Stop -GFP endo
1344
MCA2-TGD-GFP endo
57
MCA domain
3xHA
GFP
B
MCA2 Y1344Stop -GFP endo
DIC/DAPI
MCA2 Y1344Stop
MCA2/DAPI
DIC
ring
trophozoite
schizont
C
MCA2 Y1344Stop -GFP endo + mCherry-K13 epi
MCA2 / K13
Kelch13
overlap
partial overlap
no overlap
21%
20%
59%
D
MCA2 Y1344Stop -GFP endo + PhIL1mCherry epi
DIC/Hoechst
PhIL1
zoom
1µm
schizont
E
p=0.29
relative growth of 3D7 control [%]
100
50
0
MCA2 Y1344Stop
F
p=0.02
RSA parasite survival [%]
2.5
2.0
1.5
1.0
0.5
0.0
3D7
MCA2 Y1344Stop

Figure 2

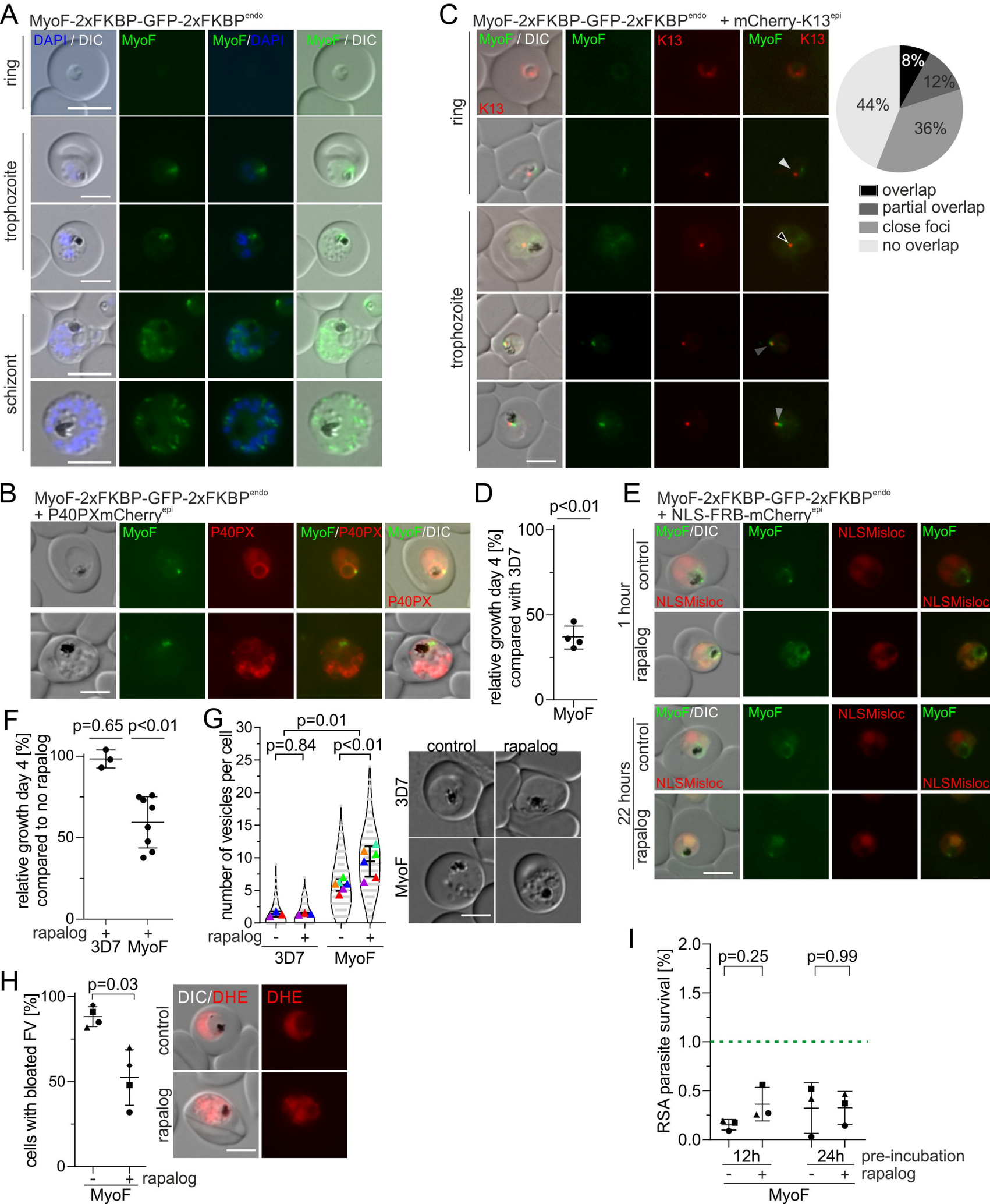
A
MyoF-2xFKBP-GFP-2xFKBP endo
DAPI / DIC
MyoF
MyoF/DAPI
MyoF / DIC
ring
trophozoite
schizont
B
MyoF-2xFKBP-GFP-2xFKBP endo
+ P40PXmCherry epi
MyoF
P40PX
MyoF/P40PX
MyoF/DIC
P40PX
C
MyoF-2xFKBP-GFP-2xFKBP endo + mCherry-K13 epi
MyoF / DIC
K13
MyoF
K13
MyoF K13
ring
trophozoite
8%
12%
44%
36%
overlap
partial overlap
close foci
no overlap
D
p<0.01
relative growth day 4 [%] compared with 3D7
100
50
0
MyoF
E
MyoF-2xFKBP-GFP-2xFKBP endo
+ NLS-FRB-mCherry epi
MyoF/DIC
MyoF
NLSMisloc
MyoF
1 hour
control
rapalog
22 hours
control
rapalog
F
p=0.65
p<0.01
relative growth day 4 [%] compared to no rapalog
100
50
0
rapalog
+
+
3D7
MyoF
G
p=0.01
p=0.84
p<0.01
number of vesicles per cell
30
25
20
15
10
5
0
rapalog
-
+
-
+
3D7
MyoF
control
rapalog
3D7
MyoF
H
p=0.03
cells with bloated FV [%]
100
50
0
-
+
rapalog
MyoF
DIC/DHE
DHE
control
rapalog
I
p=0.25
p=0.99
RSA parasite survival [%]
2.0
1.5
1.0
0.5
0.0
12h
24h
pre-incubation
-
+
-
+
rapalog
MyoF

Figure 3

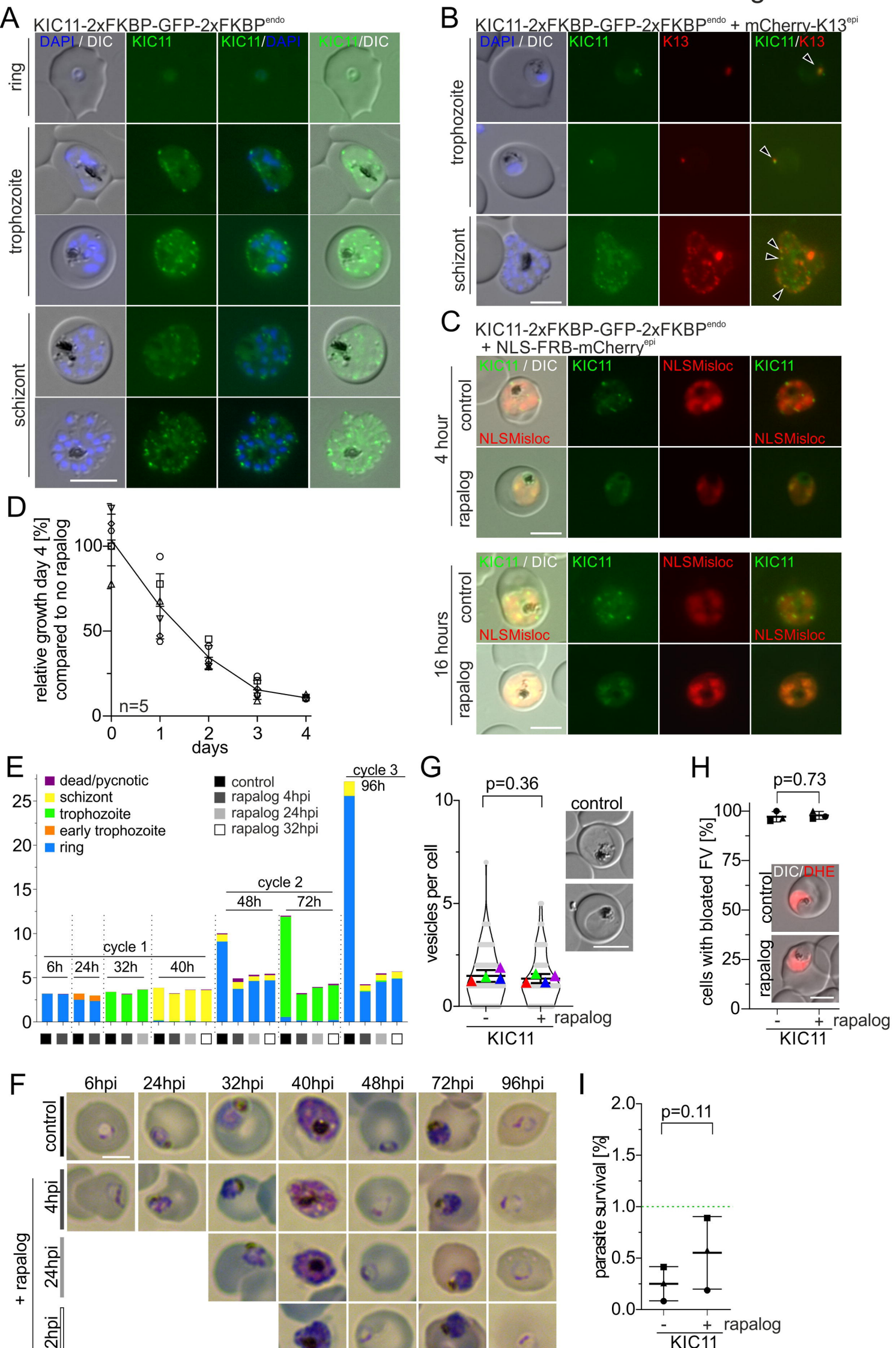
A
KIC11-2xFKBP-GFP-2xFKBP endo
DAPI / DIC
KIC11
KIC11/DAPI
KIC11/DIC
ring
trophozoite
schizont
B
KIC11-2xFKBP-GFP-2xFKBP endo + mCherry-K13 epi
DAPI / DIC
KIC11
K13
KIC11/K13
trophozoite
schizont
C
KIC11-2xFKBP-GFP-2xFKBP endo
+ NLS-FRB-mCherry epi
KIC11 / DIC
KIC11
NLSMisloc
KIC11
4 hour
control
rapalog
16 hours
control
rapalog
D
relative growth day 4 [%]
compared to no rapalog
100
50
0
n=5
0
1
2
3
4
days
E
dead/pycnotic
schizont
trophozoite
early trophozoite
ring
control
rapalog 4hpi
rapalog 24hpi
rapalog 32hpi
cycle 1
cycle 2
cycle 3
6h
24h
32h
40h
48h
72h
96h
25
20
15
10
5
0
G
p=0.36
control
vesicles per cell
10
5
0
-
+
rapalog
KIC11
H
p=0.73
cells with bloated FV [%]
100
75
50
25
0
DIC/DHE
control
rapalog
-
+
rapalog
KIC11
F
6hpi
24hpi
32hpi
40hpi
48hpi
72hpi
96hpi
control
+ rapalog
4hpi
24hpi
32hpi
I
p=0.11
parasite survival [%]
2.0
1.5
1.0
0.5
0.0
-
+
rapalog
KIC11

Figure 4

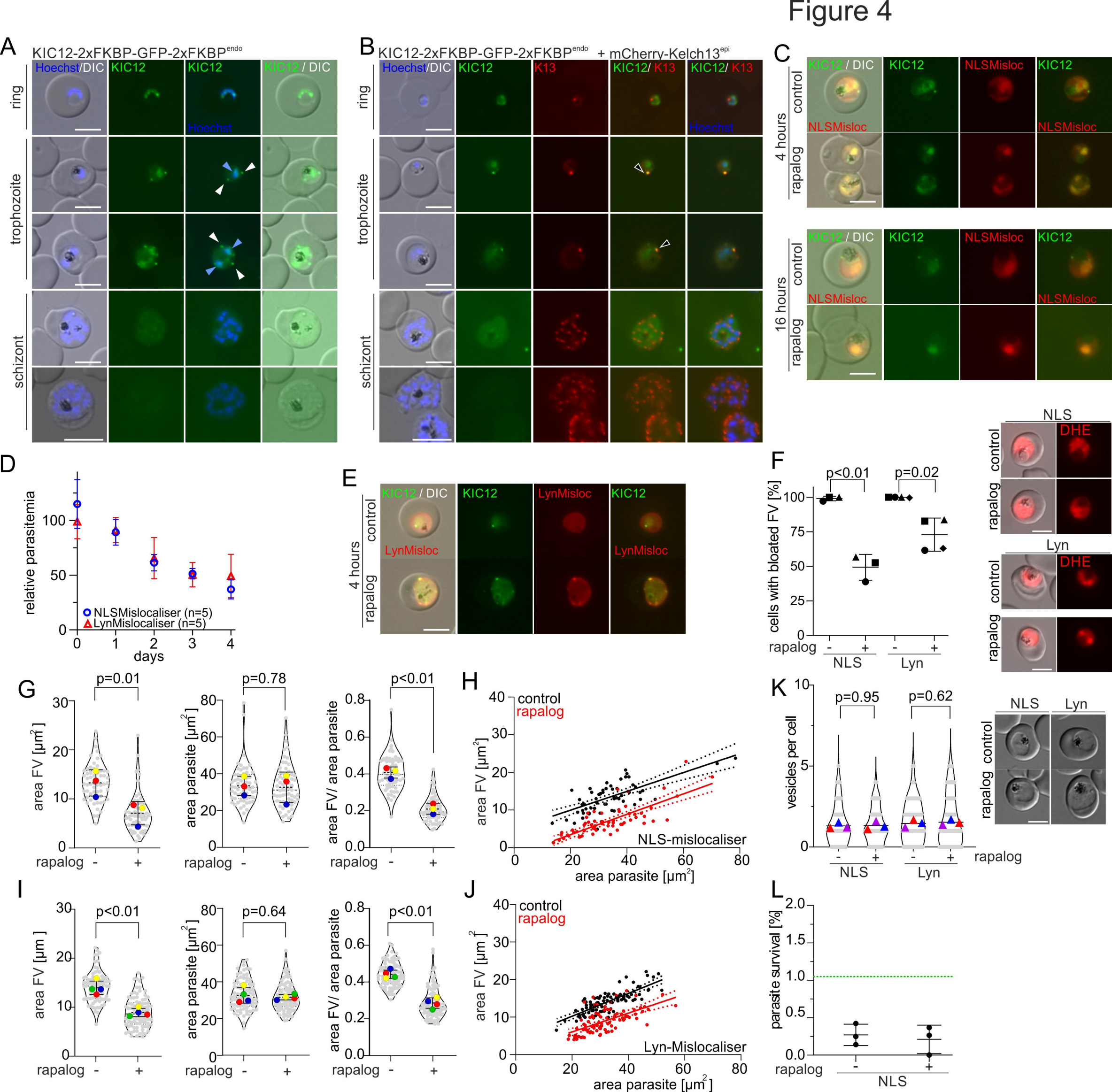
A
KIC12-2xFKBP-GFP-2xFKBP^endo
Hoechst/DIC
KIC12
KIC12 / DIC
ring
trophozoite
schizont
B
KIC12-2xFKBP-GFP-2xFKBP^endo + mCherry-Kelch13^epi
K13
KIC12/ K13
C
4 hours
16 hours
control
rapalog
NLSMisloc
D
relative parasitemia
days
NLSMislocaliser (n=5)
LynMislocaliser (n=5)
E
4 hours
LynMisloc
F
p<0.01
p=0.02
cells with bloated FV [%]
rapalog
NLS
Lyn
DHE
G
p=0.01
p=0.78
p<0.01
area FV [µm²]
area parasite [µm²]
area FV/ area parasite
H
control
rapalog
NLS-mislocaliser
area parasite [µm²]
K
p=0.95
p=0.62
vesicles per cell
I
p<0.01
p=0.64
J
Lyn-Mislocaliser
L
parasite survival [%]

Figure 5

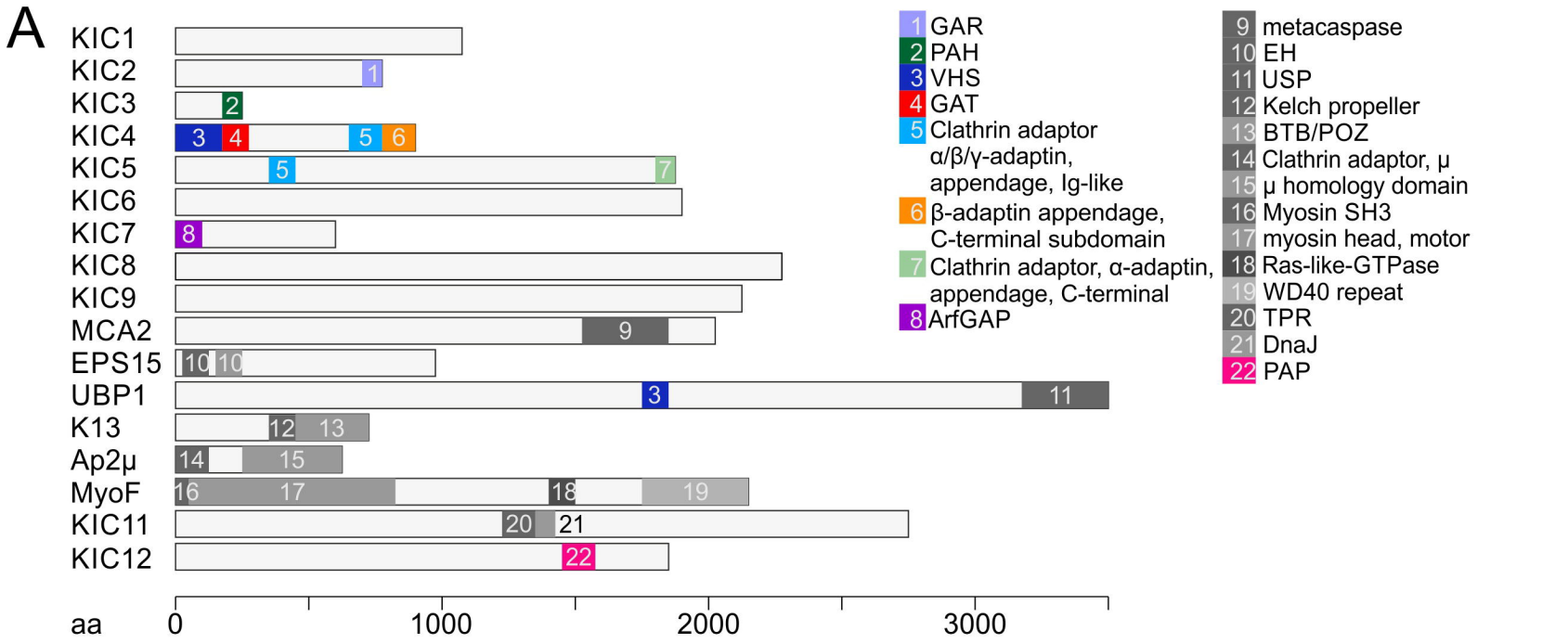

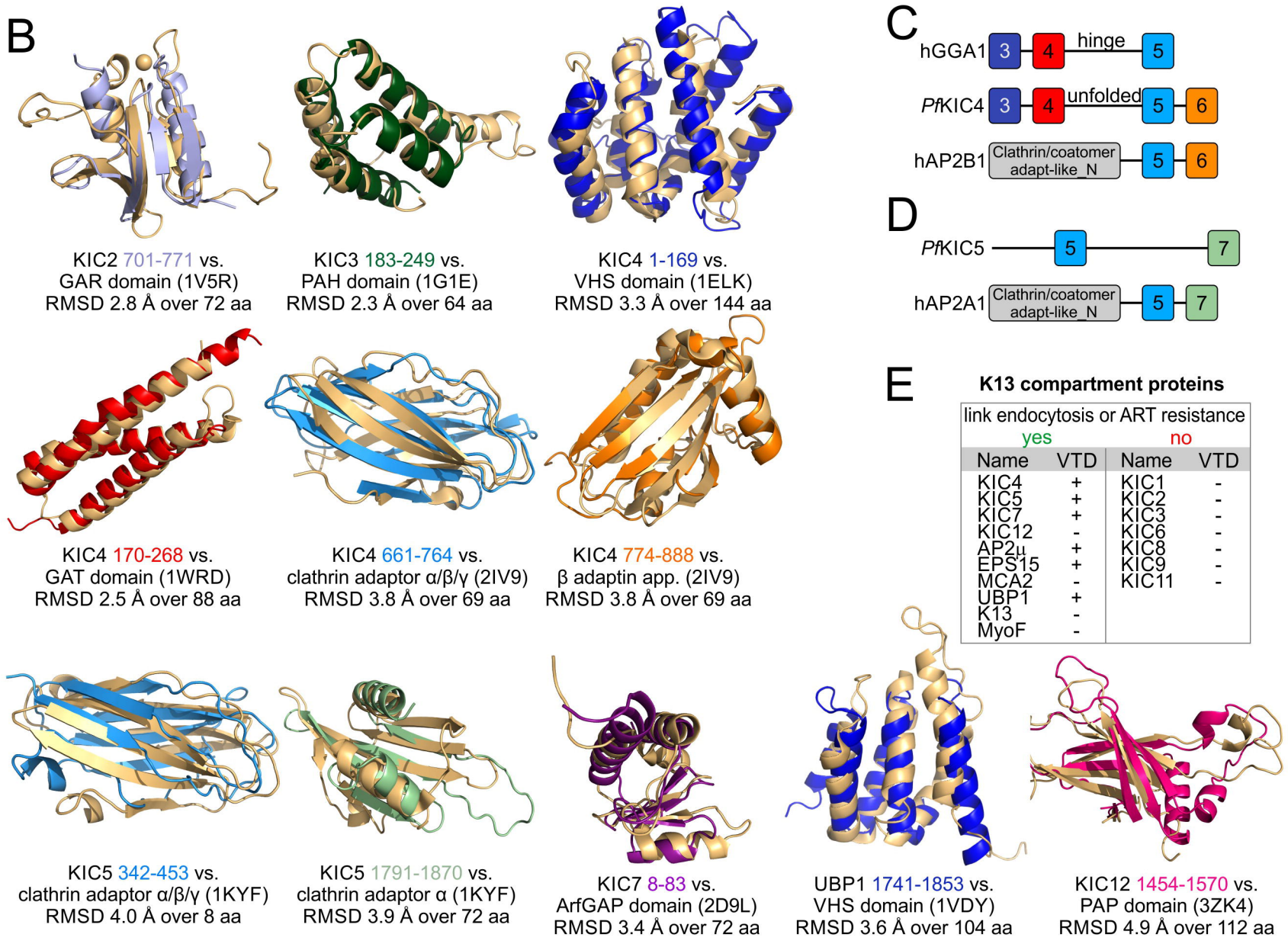

K13 compartment proteins

link endocytosis or ART resistance			
yes		no	
Name	VTD	Name	VTD
KIC4	+	KIC1	-
KIC5	+	KIC2	-
KIC7	+	KIC3	-
KIC12	-	KIC6	-
AP2µ	+	KIC8	-
EPS15	+	KIC9	-
MCA2	-	KIC11	-
UBP1	+		
K13	-		
MyoF	-		